

This is a non-peer reviewed preprint submitted to EarthArXiv.
This manuscript has been submitted for peer review.

Subsequent versions may have altered content.

Please contact Vince Cooper (vcooper@uw.edu) regarding this manuscript's content.

Last Glacial Maximum pattern effects reduce climate sensitivity estimates

Vincent T. Cooper^{1*}, Kyle C. Armour¹, Gregory J. Hakim¹, Jessica E. Tierney², Matthew B. Osman³, Cristian Proistosescu⁴, Yue Dong⁵, Natalie J. Burls⁶, Timothy Andrews⁷, Daniel E. Amrhein⁸, Jiang Zhu⁸, Wenhao Dong⁹, Yi Ming¹⁰, and Philip Chmielewicz⁴

¹ Department of Atmospheric Sciences, University of Washington, Seattle, WA, USA

² Department of Geosciences, University of Arizona, Tucson, AZ, USA

³ Department of Geography, University of Cambridge, UK

⁴ Department of Atmospheric Sciences and Department of Geology, University of Illinois at Urbana Champaign, Urbana, IL, USA

⁵ Lamont-Doherty Earth Observatory, Columbia University, Palisades, NY, USA

⁶ Department of Atmospheric, Oceanic, and Earth Sciences, George Mason University, Fairfax, VA, USA

⁷ Met Office Hadley Centre, Exeter, UK

⁸ Climate and Global Dynamics Laboratory, National Center for Atmospheric Research, Boulder, CO, USA

⁹ NOAA/Geophysical Fluid Dynamics Laboratory, Princeton, NJ, USA

¹⁰ Earth and Environmental Sciences and Schiller Institute for Integrated Science and Society, Boston College, Boston, MA, USA

***Corresponding author:** Vince Cooper (vcooper@uw.edu)

25 **Abstract**

26 The Last Glacial Maximum (LGM) provides a leading constraint^{1–3} on equilibrium climate
27 sensitivity (ECS), a measure of global-mean warming from increased greenhouse gas
28 concentrations. Recent research^{4–9} shows that feedbacks governing climate sensitivity depend on
29 the spatial pattern of sea-surface temperature (SST), a phenomenon known as the “pattern
30 effect.” Using the LGM to constrain future warming requires accurately reconstructing SST
31 patterns and quantifying how feedbacks differ between the LGM and modern-day. Here we show
32 that the climate is more sensitive to LGM forcing than modern-day CO₂ because LGM ice-sheet
33 forcing amplifies SST changes in the extratropics where feedbacks are less stabilizing. We
34 quantify this LGM pattern effect using atmospheric models combined with spatially complete
35 LGM SST reconstructions^{2,10–12} from paleoclimate data assimilation projects¹³. Revising
36 modern-day ECS to account for LGM pattern effects results in stronger constraints. Combining
37 the LGM with other lines of evidence¹, we find a modern-day ECS of 2.9°C (2.1–4.1°C, 5–95%
38 range), narrowing uncertainty compared to recent community assessments^{1,3} that did not account
39 for LGM pattern effects. Our results demonstrate the importance of accounting for SST pattern
40 effects when inferring ECS from paleoclimate periods affected by substantial non-CO₂ forcing.

41

42 **Main Text**

43 Equilibrium climate sensitivity (ECS) is the steady-state response of global-mean near-surface
44 air temperature to doubling atmospheric CO₂ above pre-industrial levels. ECS is a focus of
45 climate policy and projections³ because it governs Earth’s long-term response to anthropogenic
46 greenhouse gas changes^{1,3}. Recently, the World Climate Research Programme’s 2020 climate
47 sensitivity assessment¹ (hereafter “WCRP20”) updated the 5–95% range for ECS to 2.3–4.7°C
48 with a central estimate of 3.1°C, which informed the ‘very likely’ range of 2.0–5.0°C and central
49 estimate of 3°C in the Intergovernmental Panel on Climate Change Sixth Assessment Report
50 (“IPCC AR6”)³. This narrowing of uncertainty compared to previous assessments was achieved
51 by quantitatively combining evidence from process understanding of climate feedbacks,
52 observations over the historical record (1870–present), and paleoclimate reconstructions of past
53 cold and warm periods. Of these lines of evidence, paleoclimate data from the Last Glacial
54 Maximum (LGM), approximately 20,000 years ago, provide a leading constraint on the upper
55 bound of ECS^{1–3}.

56 Using paleoclimate data to constrain modern-day ECS requires accounting for how
57 climate feedbacks change across different climate states^{1,3,14–19}. The current assumption is that
58 colder climates are less sensitive (i.e., have more-negative feedbacks) than warmer states^{1,3,15–19}.
59 However, the simple assumption that feedbacks change with *global-mean* temperature does not
60 account for how feedbacks depend on changing *spatial patterns* of sea-surface temperature
61 (SST), a phenomenon known as the SST “pattern effect”^{4–9}.

62 A robust understanding of the SST pattern effect has been developed in the context of
63 recent warming. Over the past century, SSTs have warmed more in the tropical west Pacific and
64 less in the east Pacific and Southern Ocean^{5,20,21}. SST changes in tropical regions of deep
65 convection (e.g., the west Pacific) produce strongly negative (stabilizing) feedbacks, whereas
66 SST changes in regions with reflective low clouds (e.g., the east Pacific) or sea ice produce
67 relatively positive (destabilizing) feedbacks^{5–9,22}. This historical pattern of SST trends is
68 expected to reverse in the future as the tropical east Pacific and Southern Ocean eventually warm
69 at higher rates, producing more-positive feedbacks and a more-sensitive climate^{9,23,24}.
70 Accounting for pattern effects causes the historical record to become a weak constraint on high
71 values of ECS^{1,3,20,21}, leaving the LGM as a leading constraint on the ECS upper bound¹.

72 However, pattern effects have not been accounted for in LGM evidence for modern-day
73 ECS^{1–3,15,25}. Importantly, if the spatial pattern of SST change at the LGM differs from the pattern
74 of future warming, then the climate feedback will differ as well. Continental ice sheets are
75 responsible for approximately half of the total LGM forcing^{2,26,27} and drive distinct climate
76 responses to topography, albedo, and sea-level^{26,28–33}, suggesting that patterns of SST change at
77 the LGM may differ substantially from those in response to a modern-day doubling of CO₂.
78 Previous work acknowledged this possibility^{1,3} but did not account for LGM pattern effects
79 because no quantification had yet been made. A key question is, would accounting for LGM
80 pattern effects strengthen or weaken constraints on modern-day ECS?

81 Here we provide the first quantification of the LGM pattern effect and its uncertainty by
82 leveraging two recent advances. First, with the advent of paleoclimate data assimilation¹³,
83 spatially complete reconstructions of SST and sea ice now exist for the LGM^{2,10–12}, including
84 estimated uncertainties. Second, recent progress in quantifying pattern effects^{20,21} provides
85 methods using atmospheric general circulation models (AGCMs) to link SST patterns to climate
86 feedbacks. These advances present a new opportunity to compare SST changes at the LGM with

87 those expected under anthropogenic CO₂ forcing and to quantify resulting differences in climate
 88 feedbacks. To assess the robustness of our results, we use five AGCMs (sampling uncertainty in
 89 how feedbacks relate to SST patterns) and four reconstructions^{2,10-12} of the LGM (sampling
 90 uncertainty in SST patterns).

91

92 **Dependence of ECS on pattern effects**

93 ECS and climate feedbacks are connected through the standard model of global-mean energy
 94 balance:

$$95 \quad \Delta N = \lambda \Delta T + \Delta F, \quad (1)$$

96 where N is the top-of-atmosphere radiative imbalance; λ is the net climate feedback (negative for
 97 stable climates); T is the near-surface air temperature; and F is the “effective” radiative forcing,
 98 i.e., the change in net downward radiative flux after adjustments to imposed perturbations but
 99 excluding radiative responses to changing surface temperature^{1,3}. Differences (Δ) are relative to
 100 an equilibrium reference state, e.g., the pre-industrial period. When the forcing is a CO₂-doubling
 101 (2xCO₂) of pre-industrial values, and the climate system reaches equilibrium ($\Delta N=0$), the
 102 resulting ΔT is referred to as the ECS:

$$103 \quad \text{ECS} = -\Delta F_{2x} / \lambda_{2x}, \quad (2)$$

104 where ΔF_{2x} is the effective radiative forcing, and λ_{2x} is the net feedback for 2xCO₂. More-
 105 negative values of λ_{2x} indicate a less-sensitive climate (lower ECS).

106 Here we aim to quantify the difference in feedbacks ($\Delta\lambda$) operating in the modern climate
 107 under 2xCO₂ (λ_{2x}) and at the LGM (λ_{LGM}):

$$108 \quad \Delta\lambda = \lambda_{2x} - \lambda_{\text{LGM}}. \quad (3)$$

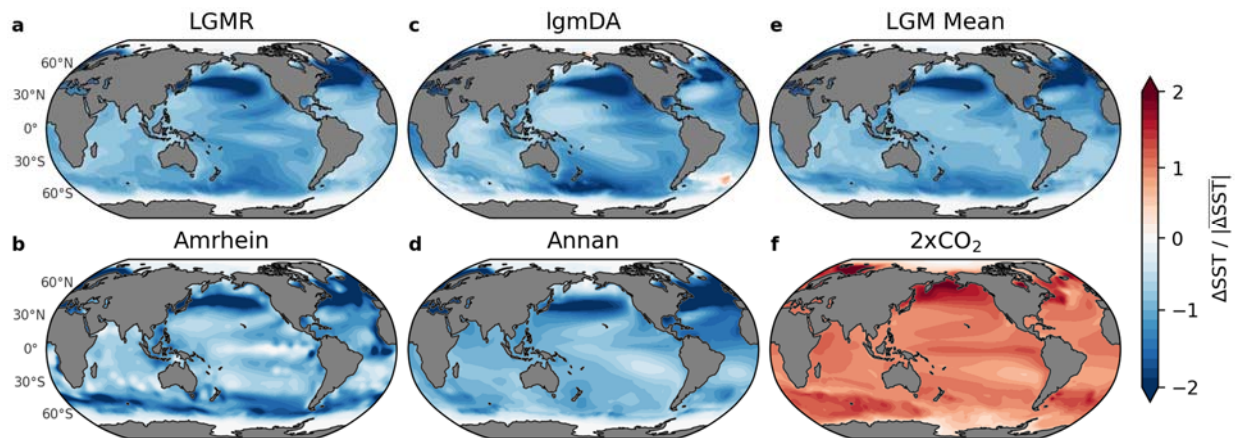
109 Following recent research on pattern effects in the historical record^{1,20,21}, we estimate λ_{2x} and
 110 λ_{LGM} using AGCM simulations with SST and sea-ice concentration (SIC) prescribed as surface
 111 boundary conditions. We further evaluate the contributions to $\Delta\lambda$ from pattern effects and global-
 112 mean temperature changes between the LGM and 2xCO₂.

113 To infer the modern-day ECS from LGM evidence, equations (2) and (3) can be
 114 combined^{1,20} to yield

$$115 \quad \text{ECS} = -\Delta F_{2x} / (\lambda_{\text{LGM}}^* + \Delta\lambda), \quad (4)$$

116 where λ_{LGM}^* is the estimate of the unadjusted LGM feedback (determined using equation (1)
 117 applied to that state), which we take from previous assessments¹⁻³, and $\Delta\lambda$ is estimated from our

118 AGCM simulations. The value of $\Delta\lambda$ depends on spatial patterns of LGM SST and SIC
 119 anomalies, for which we use state-of-the-art reconstructions^{2,10–12} based on data assimilation.
 120
 121



122
 123 **Fig. 1 | Patterns of sea-surface-temperature (SST) anomalies from data assimilation at the Last**
 124 **Glacial Maximum (LGM) compared to modern-day doubling of CO₂ (2xCO₂).** LGM reconstructions
 125 include **a**, Last Glacial Maximum Reanalysis (LGMR)¹⁰, **b**, Amrhein¹¹, **c**, lgmDA², **d**, Annan¹², and **e**, the
 126 mean of the four LGM patterns. **f**, Pattern of the multi-model mean from near-equilibrium simulations in
 127 LongRunMIP³⁴ of 2xCO₂, initialized from pre-industrial control. To show SST patterns, local SST
 128 anomalies are divided by absolute values of global-mean SST anomalies (consistent with feedbacks being
 129 radiative responses divided by temperature anomalies). All panels show annual means. LGM
 130 reconstructions are infilled to modern coastlines (Methods).
 131
 132

133 **From data assimilation to pattern effect**

134 Similar to Bayesian statistics, paleoclimate data assimilation¹³ begins with a “prior” estimate of
 135 the climate state from model ensembles. Proxy data provide indirect climate observations that
 136 update the prior, balancing relative error in the prior and the observations. This results in a
 137 “posterior” state estimate, constrained by observations and accounting for uncertainty in priors
 138 and data. Since the posterior is sensitive to priors, proxies, and methods, we sample this
 139 uncertainty³⁵ by using multiple reconstructions.

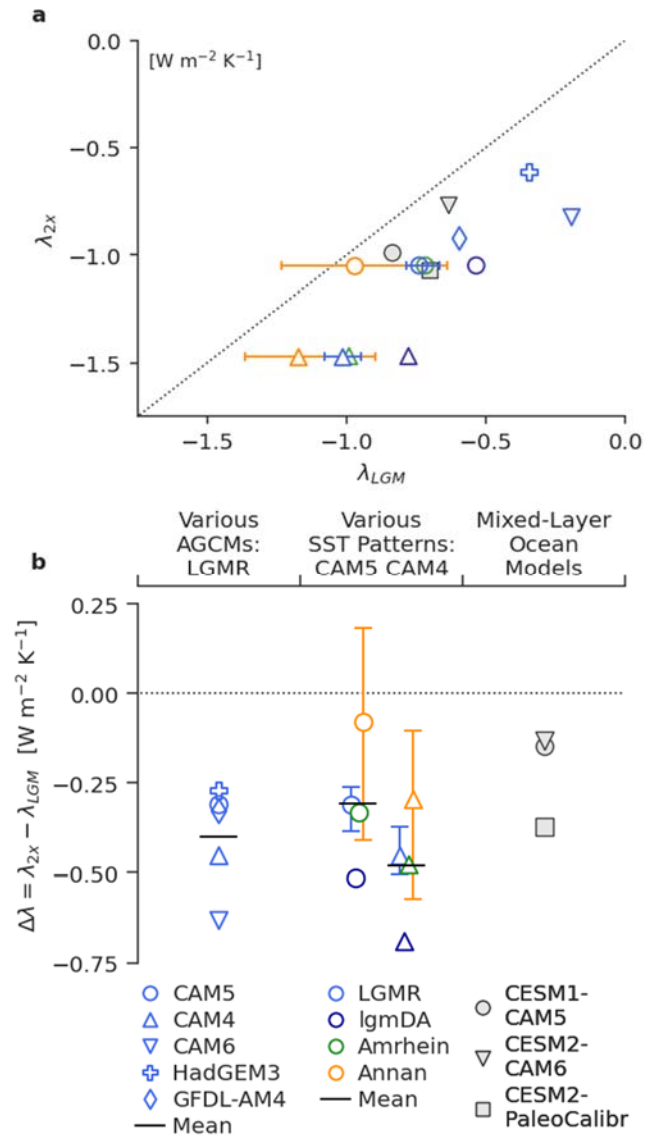
140 Figure 1 shows the four SST reconstructions (Methods) we use to quantify the LGM
 141 pattern effect. All four reconstructions have a prominent common feature: amplified extratropical
 142 cooling in both the North Pacific and North Atlantic Oceans. While the LGM reconstructions
 143 differ in other regions that are important for climate feedbacks, e.g., the tropical Pacific^{5–9} and

144 Southern Ocean^{23,36,37}, their robust agreement in the northern extratropics proves to be essential
145 for the LGM pattern effect. The zonally consistent maximum near 40°N in SST anomalies at the
146 LGM is a strong contrast with the near-equilibrium response to modern-day 2xCO₂ (Fig. 1f,
147 Extended Data Fig. 1) as simulated by climate models in LongRunMIP³⁴ (Methods), suggesting
148 the potential for feedbacks to differ between LGM and 2xCO₂ climates. Using data-constrained
149 patterns to quantify how LGM feedbacks compare to feedbacks in 2xCO₂ is a major advance
150 over past comparisons (all based on models), which have produced conflicting results^{25,26,38–42}
151 (SI Section 1).

152 We calculate net feedbacks using AGCMs with prescribed SST and SIC boundary
153 conditions. We first conduct AGCM simulations with a “baseline” pattern representing the pre-
154 industrial climate, for which we use SST and SIC in the Late Holocene (mean of 0–4,000 years
155 ago) from the Last Glacial Maximum Reanalysis¹⁰ (LGMR). We then perform AGCM
156 simulations with SST and SIC boundary conditions (Methods) from 2xCO₂ in LongRunMIP³⁴
157 and the four LGM reconstructions^{2,10–12} (SST in Fig. 1; SIC in Extended Data Fig. 2). Finally, we
158 calculate global-mean ΔN and ΔT (relative to the baseline) in each 2xCO₂ and LGM simulation,
159 which yields net feedbacks as $\lambda = \Delta N / \Delta T$ using equation (1). All forcings are held constant
160 ($\Delta F = 0$) at modern-day levels across our AGCM simulations, therefore all simulated top-of-
161 atmosphere radiation and feedbacks can be attributed solely to SST/SIC differences (Methods).

162 We find that λ_{2x} is more negative (stabilizing) than λ_{LGM} , indicating that the climate
163 system is more sensitive to LGM forcing than to 2xCO₂ (Fig. 2). We use the LGMR pattern (Fig.
164 1a) in five AGCMs (CAM4, CAM5, CAM6, GFDL-AM4, and HadGEM3-GC3.1-LL) to
165 evaluate uncertainty from atmospheric model physics, and we use all four LGM reconstructions
166 (Fig. 1a–d) in CAM4 and CAM5 to evaluate uncertainty from LGM patterns. The LGM pattern
167 effect, $\Delta\lambda$ in equation (3), is negative across all five AGCMs and all four LGM reconstructions.
168 The five AGCMs produce a mean $\Delta\lambda = -0.40 \text{ Wm}^{-2}\text{K}^{-1}$ (Fig. 2b; detailed results in SI Tables 1–
169 2). We also evaluate uncertainty in the 2xCO₂ pattern but find that this is of secondary
170 importance (Methods, Extended Data Figs. 3–4). Our main result is that the climate is more
171 sensitive to LGM forcing than it is to modern-day 2xCO₂ forcing ($\Delta\lambda < 0$), implying lower
172 estimates of modern-day ECS by equation (4), and this finding is robust despite uncertainties in
173 atmospheric physics and LGM reconstructions.

174 **Fig. 2 | Last Glacial Maximum (LGM) and**
 175 **2xCO₂ climate feedbacks and LGM pattern**
 176 **effect ($\Delta\lambda$).** Different atmospheric general
 177 circulation models (AGCMs), all using the
 178 LGMR pattern for the LGM, are indicated by
 179 symbols; different LGM patterns (in CAM5 and
 180 CAM4) are indicated by colors. Error bars for
 181 Annan and LGMR represent 1st and 4th quartiles
 182 of ensemble members (Methods); central values
 183 indicate ensemble mean. For comparison with
 184 AGCM results using LGM data assimilation, the
 185 following feedbacks (in mixed-layer ocean
 186 coupled to AGCM) from previous studies are
 187 also included: CESM1-CAM5²⁶, CESM2-
 188 CAM6⁴³, and CESM2-PaleoCalibr⁴⁴ (modified
 189 version of CAM6). **a**, Scatter plot of 2xCO₂
 190 feedbacks (λ_{2x}) versus LGM feedbacks (λ_{LGM}),
 191 with $\lambda_{2x}=\lambda_{LGM}$ shown as dotted line. **b**, LGM
 192 pattern effect, $\Delta\lambda=\lambda_{2x}-\lambda_{LGM}$, using feedbacks
 193 shown in panel **a**, with $\Delta\lambda=0$ shown as dotted
 194 line.



202 Mechanisms driving LGM pattern effects

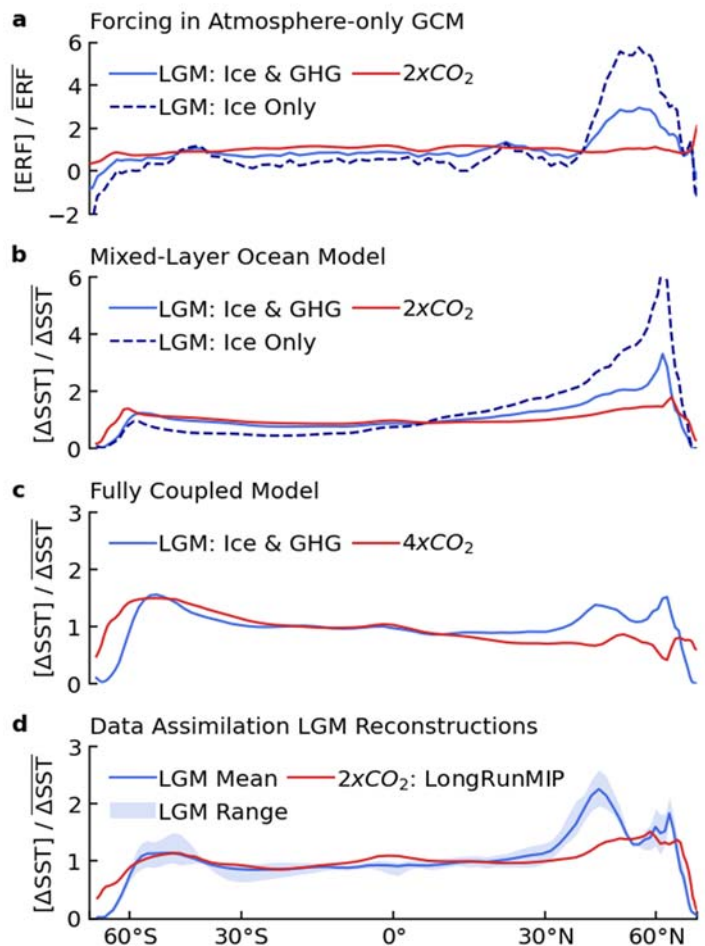
203 For comparison with our feedbacks in AGCMs driven by LGM reconstructions, we examine
 204 previously published results²⁶ from AGCMs coupled to mixed-layer (“slab”) oceans (Fig. 2),
 205 which allow SST changes in response to imposed forcings but exclude changes in ocean
 206 dynamics⁴⁵. These mixed-layer-model versions of CESM1-CAM5²⁶, CESM2-CAM6⁴³, and
 207 CESM2-PaleoCalibr⁴⁴ (using a modified CAM6), which differ from our AGCM experiments by
 208 including forcings from ice sheets and greenhouse gases, also produce $\Delta\lambda < 0$. Although
 209 disagreements in SST patterns compared to proxy data suggest that free-running coupled models

210 cannot reliably estimate the value of $\Delta\lambda$, the models demonstrate the physical mechanisms
 211 linking patterns of forcing, SST response, and climate feedbacks.

212 Comparing zonal-mean patterns of effective radiative forcing and SST changes from
 213 CESM1-CAM5 simulations²⁶ under 2xCO₂ forcing, LGM forcing (ice sheet and GHG), and
 214 LGM ice-sheet forcing alone (including coastline changes) emphasizes that localized ice-sheet
 215 forcing causes the amplified SST response in the northern extratropics at the LGM compared to
 216 2xCO₂ (Fig. 3a–c). Differences in SST responses between LGM and 2xCO₂ persist at quasi-
 217 equilibrium in a fully coupled (atmosphere–ocean GCM) version of CESM1-CAM5 (Fig. 3c,
 218 Extended Data Fig. 5). Comparing the fully coupled model’s response to LGM forcing (Figure
 219 3c) with the data-assimilation patterns we use to quantify pattern effects (Fig. 3d) suggests that
 220 LGM ice sheets amplify SST cooling in the northern extratropics^{26,32,33} but that this pattern is
 221 more pronounced in proxy reconstructions.

222

223 **Fig. 3 | Zonal-mean patterns of effective**
 224 **radiative forcing (ERF) and sea-surface-**
 225 **temperature (SST) anomalies.** All
 226 anomalies are normalized through division
 227 by global-mean anomalies. **a–c**, Model
 228 simulations in CESM1-CAM5 from Zhu &
 229 Poulsen²⁶. **a**, ERF directly from three
 230 fixed-SST simulations using atmospheric
 231 general circulation model with LGM
 232 greenhouse-gas (GHG) and ice-sheet (Ice)
 233 forcing, 2xCO₂, and LGM ice-sheet
 234 forcing alone²⁶ (including coastline
 235 changes). **b**, Equilibrium SST patterns
 236 (corresponding to **a**) in coupled mixed-
 237 layer ocean model. **c**, Quasi-equilibrium
 238 SST patterns from fully coupled
 239 atmosphere-ocean model, comparing LGM
 240 forcings²⁶ with abrupt-4xCO₂ forcing⁴⁶ (no
 241 long-run 2xCO₂ simulation is available).
 242 Note vertical-axis scales. **d**, Mean and
 243 range of SST patterns from four data-
 244 assimilation reconstructions^{2,10–12} of the
 245 LGM compared to 2xCO₂ multi-model
 246 mean from LongRunMIP³⁴ (six near-
 247 equilibrium simulations of 700-4500
 248 years).



249 Decomposing λ from our AGCM simulations into component feedbacks (Extended Data
250 Fig. 6), including results from direct model output and from radiative kernels (Methods), shows
251 that shortwave cloud feedbacks are responsible for much of the negative value of $\Delta\lambda$ and for
252 much of the spread across AGCMs. The combined feedback from lapse rate and water vapor
253 changes also contributes to negative values of $\Delta\lambda$, while surface albedo offsets the net difference
254 with a positive $\Delta\lambda$. These results align with previous studies that emphasize cloud and lapse-rate
255 changes in pattern effects^{6,7,9,24}.

256 Spatial distributions of feedbacks (Extended Data Fig. 7, SI Section 5) clarify the
257 connection between ice-sheet forcing, SST response, and cloud feedbacks. Where the SST
258 cooling from LGM ice sheets is amplified in the North Pacific and North Atlantic, positive
259 shortwave cloud feedbacks are prominent due to increases in reflective low clouds^{5-9,22,33}.
260 Compared to 2xCO₂ simulations, LGM reconstructions have relatively small SST anomalies in
261 tropical ascent regions (Extended Data Fig. 1) where feedbacks are most negative^{5-8,22,36}. The
262 result is that the LGM SST pattern produces a less-negative global climate feedback compared to
263 the 2xCO₂ SST pattern and $\Delta\lambda < 0$.

264

265 **Pattern and temperature dependence**

266 While our explanation for feedback differences between LGM and 2xCO₂ forcing focuses on
267 SST pattern differences, we also estimate how $\Delta\lambda$ is affected by global-mean temperature within
268 our AGCM simulations. We consider that

$$269 \quad \Delta\lambda \approx \Delta\lambda_{\text{PatternOnly}} + \Delta\lambda_T, \quad (5)$$

270 where $\Delta\lambda_{\text{PatternOnly}}$ is the feedback change due to different patterns of SST anomalies and $\Delta\lambda_T$ is
271 the feedback change due to different global-mean temperatures (T). Recent community
272 assessments^{1,3} assume warmer climates are more sensitive ($\Delta\lambda_T > 0$)^{15-19,39}, which is at odds with
273 the total $\Delta\lambda < 0$ we find for the LGM in AGCMs and coupled models (Fig. 2).

274 To separate pattern effects from temperature dependence, we perform additional “pattern-
275 only” simulations in CAM4, CAM5, and CAM6 using the LGMR and 2xCO₂ patterns. For these
276 simulations, we multiply local SST anomalies by constant scaling factors to yield global-mean
277 $\Delta\text{SST} = -0.5$ K with constant baseline SIC (Methods). SST scaling preserves spatial patterns of
278 anomalies but forces global-mean ΔT to be small and equal across simulations, i.e., $\Delta\lambda_T \approx 0$ in the
279 pattern-only simulations. We then repeat the feedback calculations, computing $\Delta\lambda_{\text{PatternOnly}}$ as in

280 equation (3). We estimate the temperature dependence $\Delta\lambda_T$ as the residual difference between the
281 main and pattern-only AGCM simulations, rearranging equation (5) to $\Delta\lambda_T \approx \Delta\lambda - \Delta\lambda_{\text{PatternOnly}}$
282 (Methods).

283 The magnitude and sign of $\Delta\lambda_T$ is found to be model-dependent, in agreement with recent
284 multi-model assessments^{25,47}, but $\Delta\lambda_T$ appears to be positive and directionally consistent with
285 current assumptions^{1,3} for feedback temperature dependence. However, $\Delta\lambda_{\text{PatternOnly}}$ is negative
286 and larger than $\Delta\lambda_T$ such that total $\Delta\lambda < 0$ in each AGCM (Extended Data Fig. 8, SI Table 3).
287 These results suggest that total $\Delta\lambda$ for the LGM is mostly attributable to SST pattern effects, and
288 $\Delta\lambda_T$ plays a smaller role over this range of climates. Recent assessments^{1,3} considered $\Delta\lambda_T$ for the
289 LGM but did not account for the larger, opposing term, $\Delta\lambda_{\text{PatternOnly}}$. The substantial LGM pattern
290 effect found here motivates revising the LGM evidence for modern-day ECS.

291

292 **ECS accounting for LGM pattern effects**

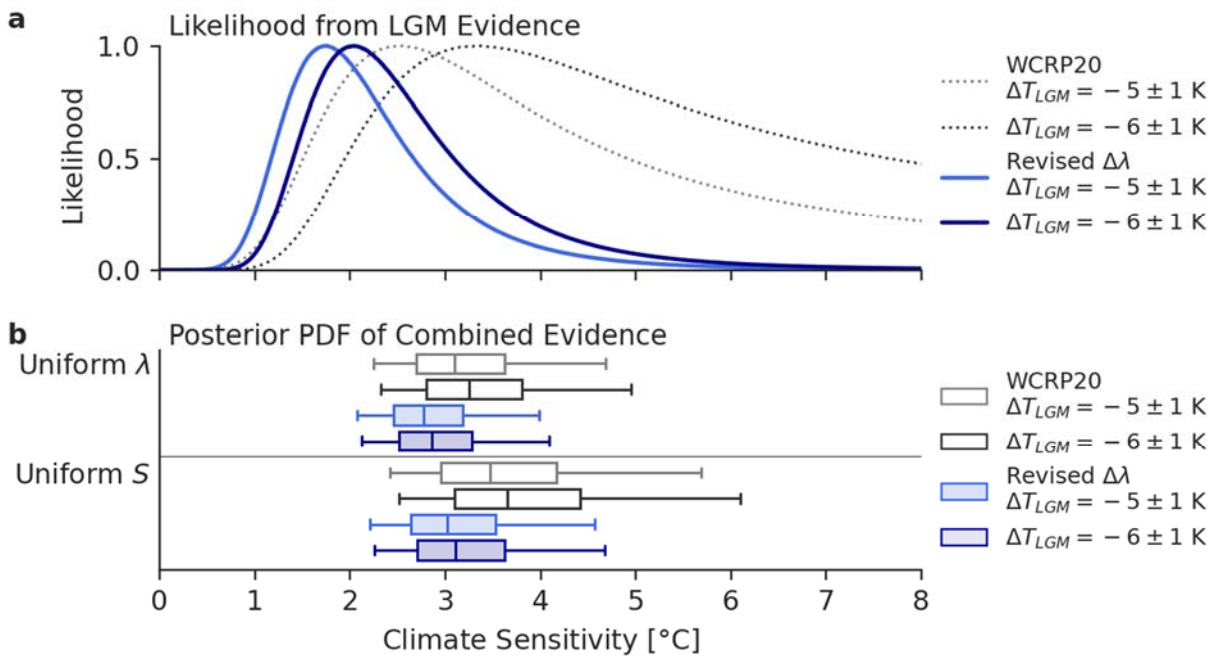
293 Constraining modern-day ECS with paleoclimate evidence requires accounting for how forcings
294 and feedbacks differ in paleoclimates relative to the modern-day $2\times\text{CO}_2$ scenario^{1,3,15}. LGM
295 inferences of ECS begin with applying equation (1) to the LGM in equilibrium, estimating the
296 unadjusted LGM feedback as $\lambda_{\text{LGM}}^* = \frac{-\sum\Delta F}{\Delta T}$. Effective radiative forcings (ΔF) include not only
297 CO_2 but also ice sheets (including sea level) and, depending on the timescale chosen for ECS¹⁻
298 ^{3,15}, additional changes that behave distinctly at the LGM: vegetation, dust, N_2O , and CH_4
299 (Methods). Finally, λ_{LGM}^* must be adjusted for differences in feedbacks ($\Delta\lambda$) relative to those
300 operating in modern-day $2\times\text{CO}_2$, following equation (4). Note that $\Delta\lambda$ captures the impact of
301 forcing efficacy⁴⁸, which does not need to be included separately in this framework (SI Section
302 1).

303 To demonstrate the impact of LGM pattern effects, we follow methods in WCRP20¹ and
304 focus on the 150-year timescale of climate sensitivity (S) applicable to modern warming^{1,3}
305 (Methods). We use WCRP20 because that assessment uniquely allows updates of individual
306 parameters and quantitatively combines lines of evidence, but our results would have the same
307 directional impact on other assessments^{2,3}. We use forcing values from WCRP20 to estimate the
308 unadjusted LGM feedback, λ_{LGM}^* in equation (4). However, given emerging evidence^{2,3,10,49} after
309 WCRP20, we report results using a global temperature anomaly for the LGM of $\Delta T_{\text{LGM}} = -6 \pm 1$ K
310 in addition to WCRP20's value of -5 ± 1 K. We implement our key finding by updating the LGM

311 total $\Delta\lambda$, which includes LGM pattern effects for the first time. We assign a Normal distribution
 312 to $\Delta\lambda$, $N(\mu=-0.37, \sigma=0.23) \text{ Wm}^{-2}\text{K}^{-1}$, reflecting spread across AGCMs and SST reconstructions
 313 (Methods). We include additional uncertainty tests in Extended Data Figures 4 and 9,
 314 demonstrating that our general conclusions hold if the assumed σ for $\Delta\lambda$ is doubled.

315 Accounting for the LGM pattern effect reduces climate sensitivity inferred from LGM
 316 evidence (Fig. 4). With $\Delta T_{\text{LGM}} \approx -6 \text{ K}$, maximum likelihood for S from the LGM evidence alone
 317 becomes 2.0 K (change of -1.3 K). Combining the updated LGM evidence with existing
 318 likelihoods for the other lines of evidence (process understanding, historical record, and
 319 Pliocene) yields new Bayesian posterior probability distributions for the two priors in WCRP20:
 320 uniform in λ (WCRP20's "Baseline") and uniform in S (a robustness test).

321
 322



323
 324

325 **Fig. 4 | Inference of modern-day climate sensitivity including the LGM pattern effect.** Results from
 326 WCRP20¹ with no LGM pattern effects and original assumption of $\Delta T_{\text{LGM}} \sim N(\mu=-5, \sigma=1) \text{ K}$ (gray) and
 327 with revised $\Delta T_{\text{LGM}} \sim N(-6, 1) \text{ K}$ (black) based on IPCC AR6³. Revised climate sensitivity including LGM
 328 pattern effects from this study (light and dark blue) assuming $\Delta\lambda \sim N(\mu=-0.37, \sigma=0.23) \text{ Wm}^{-2}\text{K}^{-1}$. Climate
 329 sensitivity shown is effective sensitivity (S) representing 150-year response, as in WCRP20¹. **a**,
 330 Likelihood functions for S based on only the LGM line of evidence. **b**, Posterior PDF after combining
 331 LGM with other lines of evidence, assuming a uniform- λ prior (upper panel) or a uniform- S prior (lower
 332 panel). Outlier lines indicate 5–95th percentiles while box indicates 25–75th percentiles and median.

333 The impact of the LGM pattern effect on the combined evidence is most pronounced on
334 the upper bound of S , which has been notoriously difficult to constrain⁵⁰. Assuming
335 $\Delta T_{LGM} \approx -6 \pm 1$ K, the posterior 95th percentile becomes 4.1 K (change of -0.9 K) with a uniform- λ
336 prior or 4.7 K (change of -1.4 K) with a uniform- S prior. The lower bound is relatively
337 unchanged at 2.1 K (uniform- λ) or 2.3 K (uniform- S). The central estimate, represented by the
338 median S , becomes 2.9 K (change of -0.4 K) with a uniform- λ prior or 3.1 K (change of -0.6 K)
339 with a uniform- S prior. These results place S in the range of 2.1–4.1°C (5–95%) for a uniform- λ
340 prior and 2.3–4.7°C (5–95%) for a uniform- S prior, indicating stronger constraints than
341 WCRP20¹ even after allowing for more glacial cooling. While the qualitative assessment in
342 IPCC AR6³ cannot be quantitatively updated, these results suggest stronger constraints on
343 modern-day ECS than assessed there as well.

344 Accounting for LGM pattern effects—enabled by recent advances in LGM SST
345 reconstruction using paleoclimate data assimilation and in quantifying pattern effects using
346 atmospheric models—provides a tighter upper bound on modern-day ECS. While each line of
347 evidence will surely evolve as scientific understanding improves, the results presented here
348 demonstrate that pattern effects must be accounted for when inferring modern-day climate
349 sensitivity from paleoclimate periods that are substantially affected by non-CO₂ forcing.

350
351

352 References

- 353 1. Sherwood, S. C. *et al.* An Assessment of Earth’s Climate Sensitivity Using Multiple Lines of
354 Evidence. *Reviews of Geophysics* **58**, (2020).
- 355 2. Tierney, J. E. *et al.* Glacial cooling and climate sensitivity revisited. *Nature* **584**, 569–573 (2020).
- 356 3. Forster, P. *et al.* 2021: The Earth’s energy budget, climate feedbacks, and climate sensitivity. in
357 *Climate Change 2021: The Physical Science Basis. Contribution of Working Group I to the Sixth*
358 *Assessment Report of the Intergovernmental Panel on Climate Change* (eds. Masson-Delmotte, V. *et*
359 *al.*) (Cambridge Univ. Press, 2021). doi:10.1017/9781009157896.009.
- 360 4. Armour, K. C., Bitz, C. M. & Roe, G. H. Time-Varying Climate Sensitivity from Regional
361 Feedbacks. *J Clim* **26**, 4518–4534 (2013).
- 362 5. Dong, Y., Proistosescu, C., Armour, K. C. & Battisti, D. S. Attributing Historical and Future
363 Evolution of Radiative Feedbacks to Regional Warming Patterns using a Green’s Function Approach:
364 The preeminence of the Western Pacific. *J Clim* (2019) doi:10.1175/JCLI-D-18-0843.1.
- 365 6. Zhou, C., Zelinka, M. D. & Klein, S. A. Impact of decadal cloud variations on the Earth’s energy
366 budget. *Nat Geosci* **9**, 871–874 (2016).
- 367 7. Andrews, T. & Webb, M. J. The Dependence of Global Cloud and Lapse Rate Feedbacks on the
368 Spatial Structure of Tropical Pacific Warming. *J Clim* **31**, 641–654 (2018).

- 369 8. Fueglistaler, S. Observational Evidence for Two Modes of Coupling Between Sea Surface
370 Temperatures, Tropospheric Temperature Profile, and Shortwave Cloud Radiative Effect in the
371 Tropics. *Geophys Res Lett* **46**, 9890–9898 (2019).
- 372 9. Ceppi, P. & Gregory, J. M. Relationship of tropospheric stability to climate sensitivity and Earth’s
373 observed radiation budget. *Proc Natl Acad Sci U S A* **114**, 13126–13131 (2017).
- 374 10. Osman, M. B. *et al.* Globally resolved surface temperatures since the Last Glacial Maximum. *Nature*
375 **599**, 239–244 (2021).
- 376 11. Amrhein, D. E., Wunsch, C., Marchal, O. & Forget, G. A Global Glacial Ocean State Estimate
377 Constrained by Upper-Ocean Temperature Proxies. *J Clim* **31**, 8059–8079 (2018).
- 378 12. Annan, J. D., Hargreaves, J. C. & Mauritsen, T. A new global surface temperature reconstruction for
379 the Last Glacial Maximum. *Climate of the Past* **18**, 1883–1896 (2022).
- 380 13. Hakim, G. J. *et al.* The last millennium climate reanalysis project: Framework and first results.
381 *Journal of Geophysical Research: Atmospheres* **121**, 6745–6764 (2016).
- 382 14. Manabe, S. & Bryan, K. CO₂-induced change in a coupled ocean-atmosphere model and its
383 paleoclimatic implications. *J Geophys Res* **90**, 11689 (1985).
- 384 15. PALAEOSENS Project Members. Making sense of palaeoclimate sensitivity. *Nature* **491**, 683–691
385 (2012).
- 386 16. Köhler, P., de Boer, B., von der Heydt, A. S., Stap, L. B. & van de Wal, R. S. W. On the state
387 dependency of the equilibrium climate sensitivity during the last 5 million years. *Climate of the Past*
388 **11**, 1801–1823 (2015).
- 389 17. von der Heydt, A. S. *et al.* Lessons on Climate Sensitivity From Past Climate Changes. *Curr Clim*
390 *Change Rep* **2**, 148–158 (2016).
- 391 18. Friedrich, T., Timmermann, A., Tigchelaar, M., Timm, O. E. & Ganopolski, A. Nonlinear climate
392 sensitivity and its implications for future greenhouse warming. *Sci Adv* **2**, (2016).
- 393 19. Rohling, E. J. *et al.* Comparing Climate Sensitivity, Past and Present. *Ann Rev Mar Sci* **10**, 261–288
394 (2018).
- 395 20. Andrews, T. *et al.* Accounting for Changing Temperature Patterns Increases Historical Estimates of
396 Climate Sensitivity. *Geophys Res Lett* **45**, 8490–8499 (2018).
- 397 21. Andrews, T. *et al.* On the Effect of Historical SST Patterns on Radiative Feedback. *Journal of*
398 *Geophysical Research: Atmospheres* **127**, (2022).
- 399 22. Zhou, C., Zelinka, M. D. & Klein, S. A. Analyzing the dependence of global cloud feedback on the
400 spatial pattern of sea surface temperature change with a Green’s function approach. *J Adv Model*
401 *Earth Syst* **9**, 2174–2189 (2017).
- 402 23. Armour, K. C., Marshall, J., Scott, J. R., Donohoe, A. & Newsom, E. R. Southern Ocean warming
403 delayed by circumpolar upwelling and equatorward transport. *Nat Geosci* **9**, 549–554 (2016).
- 404 24. Dong, Y. *et al.* Intermodel Spread in the Pattern Effect and Its Contribution to Climate Sensitivity in
405 CMIP5 and CMIP6 Models. *J Clim* **33**, 7755–7775 (2020).
- 406 25. Renoult, M., Sagoo, N., Zhu, J. & Mauritsen, T. Causes of the weak emergent constraint on climate
407 sensitivity at the Last Glacial Maximum. *Climate of the Past* **19**, 323–356 (2023).
- 408 26. Zhu, J. & Poulsen, C. J. Last Glacial Maximum (LGM) climate forcing and ocean dynamical
409 feedback and their implications for estimating climate sensitivity. *Climate of the Past* **17**, 253–267
410 (2021).
- 411 27. Braconnot, P. & Kageyama, M. Shortwave forcing and feedbacks in Last Glacial Maximum and Mid-
412 Holocene PMIP3 simulations. *Philosophical Transactions of the Royal Society A: Mathematical,*
413 *Physical and Engineering Sciences* **373**, 20140424 (2015).
- 414 28. Manabe, S. & Broccoli, A. J. The influence of continental ice sheets on the climate of an ice age. *J*
415 *Geophys Res* **90**, 2167 (1985).
- 416 29. Cook, K. H. & Held, I. M. Stationary Waves of the Ice Age Climate. *J Clim* **1**, 807–819 (1988).
- 417 30. Lee, S.-Y., Chiang, J. C. H. & Chang, P. Tropical Pacific response to continental ice sheet
418 topography. *Clim Dyn* **44**, 2429–2446 (2015).

- 419 31. DiNezio, P. N. *et al.* Glacial changes in tropical climate amplified by the Indian Ocean. *Sci Adv* **4**,
420 (2018).
- 421 32. Roberts, W. H. G., Li, C. & Valdes, P. J. The Mechanisms that Determine the Response of the
422 Northern Hemisphere’s Stationary Waves to North American Ice Sheets. *J Clim* **32**, 3917–3940
423 (2019).
- 424 33. Amaya, D. J. *et al.* Air-sea coupling shapes North American hydroclimate response to ice sheets
425 during the Last Glacial Maximum. *Earth Planet Sci Lett* **578**, (2022).
- 426 34. Rugenstein, M. *et al.* LongRunMIP: Motivation and Design for a Large Collection of Millennial-
427 Length AOGCM Simulations. *Bull Am Meteorol Soc* **100**, 2551–2570 (2019).
- 428 35. Amrhein, D. E., Hakim, G. J. & Parsons, L. A. Quantifying Structural Uncertainty in Paleoclimate
429 Data Assimilation With an Application to the Last Millennium. *Geophys Res Lett* **47**, (2020).
- 430 36. Kang, S. M. & Xie, S. P. Dependence of Climate Response on Meridional Structure of External
431 Thermal Forcing. *J Clim* **27**, 5593–5600 (2014).
- 432 37. Rose, B. E. J. *et al.* The dependence of transient climate sensitivity and radiative feedbacks on the
433 spatial pattern of ocean heat uptake. *Geophys Res Lett* **41**, 1071–1078 (2014).
- 434 38. Crucifix, M. Does the Last Glacial Maximum constrain climate sensitivity? *Geophys Res Lett* **33**,
435 L18701 (2006).
- 436 39. Yoshimori, M., Hargreaves, J. C., Annan, J. D., Yokohata, T. & Abe-Ouchi, A. Dependency of
437 Feedbacks on Forcing and Climate State in Physics Parameter Ensembles. *J Clim* **24**, 6440–6455
438 (2011).
- 439 40. Stap, L. B., Köhler, P. & Lohmann, G. Including the efficacy of land ice changes in deriving climate
440 sensitivity from paleodata. *Earth System Dynamics* **10**, 333–345 (2019).
- 441 41. Shakun, J. D. Modest global-scale cooling despite extensive early Pleistocene ice sheets. *Quat Sci*
442 *Rev* **165**, 25–30 (2017).
- 443 42. Hopcroft, P. O. & Valdes, P. J. How well do simulated last glacial maximum tropical temperatures
444 constrain equilibrium climate sensitivity? *Geophys Res Lett* **42**, 5533–5539 (2015).
- 445 43. Zhu, J. *et al.* Assessment of Equilibrium Climate Sensitivity of the Community Earth System Model
446 Version 2 Through Simulation of the Last Glacial Maximum. *Geophys Res Lett* **48**, (2021).
- 447 44. Zhu, J. *et al.* LGM Paleoclimate Constraints Inform Cloud Parameterizations and Equilibrium
448 Climate Sensitivity in CESM2. *J Adv Model Earth Syst* **14**, e2021MS002776 (2022).
- 449 45. Bitz, C. M. *et al.* Climate Sensitivity of the Community Climate System Model, Version 4. *J Clim* **25**,
450 3053–3070 (2012).
- 451 46. Zhu, J., Poulsen, C. J. & Tierney, J. E. Simulation of Eocene extreme warmth and high climate
452 sensitivity through cloud feedbacks. *Sci Adv* **5**, (2019).
- 453 47. Bloch-Johnson, J. *et al.* Climate Sensitivity Increases Under Higher CO₂ Levels Due to Feedback
454 Temperature Dependence. *Geophys Res Lett* **48**, e2020GL089074 (2021).
- 455 48. Zhou, C. *et al.* Explaining Forcing Efficacy With Pattern Effect and State Dependence. *Geophys Res*
456 *Lett* **50**, (2023).
- 457 49. Seltzer, A. M. *et al.* Widespread six degrees Celsius cooling on land during the Last Glacial
458 Maximum. *Nature* **593**, 228–232 (2021).
- 459 50. Knutti, R. & Hegerl, G. C. The equilibrium sensitivity of the Earth’s temperature to radiation
460 changes. *Nat Geosci* **1**, 735–743 (2008).
- 461

462 **Methods**

463 **Data-assimilation reconstructions of the LGM**

464 We use four LGM reconstructions to quantify the LGM pattern effect, sampling uncertainty³⁵
465 across data assimilation methods and model priors⁵¹. Osman et al. (2021) produced the time-
466 dependent Last Glacial Maximum Reanalysis¹⁰ (“LGMR”) spanning the past 24,000 years; the
467 SST and SIC fields that represent the LGM in their reanalysis are time means spanning 19,000–
468 23,000 years ago. Tierney et al. (2020)² produced the state estimate “lgmDA” dataset. Both the
469 LGMR and lgmDA use priors from isotope-enabled simulations in iCESM1.2 and iCESM1.3
470 with assimilation of seasonal and annual SST proxies in an ensemble Kalman filter; there are
471 differences in the proxy databases and methods between the two reconstructions. Annan et al.
472 (2022)¹² also used an ensemble Kalman filter but with a multi-model prior, including 19
473 ensemble members from a wide array of climate models spanning PMIP2 (launched in 2002) to
474 PMIP4 (launched in 2017); they assimilated annual SST proxies and land-temperature proxies;
475 they also applied an adjustment to the prior ensemble to pre-center the prior around available
476 proxy data. Amrhein et al. (2018)¹¹ fit the MITgcm ocean model to seasonal and annual SST
477 proxies⁵² using least-squares with Lagrange multipliers by adjusting prior atmospheric fields
478 from a CCSM4 LGM simulation⁵³.

479

480 **Simulations with atmospheric general circulation models (AGCMs)**

481 SST/SIC boundary conditions (BCs) for the LGM, Late Holocene baseline, and 2xCO₂ are
482 prepared to maintain constant forcing, i.e., $\Delta F=0$ in equation (1), across simulations. Topography
483 is held constant, i.e., the LGM ice sheets are not present in AGCM simulations because their
484 impact is already included as a forcing, and we are isolating feedbacks from changing SST/SIC.

485 For the LGM and Late Holocene datasets, we adjust for differences relative to modern
486 coastlines, determined from ref.^{54,55}, using kriging and extrapolation near coastlines in polar
487 regions (details in SI Section 3). While sea-level changes must be neutralized to preserve $\Delta F=0$
488 in the AGCM simulations, infilling SST over the Sunda Shelf represents a notable
489 uncertainty^{31,56}. The alternative option, holding all forcings constant at LGM rather than modern
490 values, would require changing modern topography to include LGM ice sheets and inherit sea
491 level of the LGM. Those changes could introduce more uncertainty in estimates of λ that are

492 relevant to future warming. Here we only consider the framework with constant modern-day
493 forcings. Further details of sea-level adjustments are provided in SI Section 3.

494 The 2xCO₂ BC is the multi-model mean of 200 years from the end of six 2xCO₂
495 simulations, initialized from pre-industrial control states, in LongRunMIP³⁴: CESM1.0.4⁵⁷ (years
496 2300-2500), CNRM-CM6-1⁵⁸ (years 550-750), HadCM3L⁵⁹ (years 500-700), MPI-ESM-1.2⁶⁰
497 (years 800-1000), GFDL-ESM2M⁶¹ (years 4300-4500), and MIROC3.2^{62,63} (years 1803-2003).
498 These simulations are near equilibrium but only represent an estimate of the true equilibrium
499 SST response to 2xCO₂.

500 The Late Holocene, defined as the climatological mean of 0–4,000 years ago in the
501 LGMR¹⁰, is used as the baseline SST/SIC for all feedback calculations. This baseline represents
502 a long-term mean of the pre-industrial climate, constrained by assimilation of proxy data. After
503 adjusting for modern sea level, the four LGM BCs and the 2xCO₂ BC for SST are prepared by
504 adding the SST anomalies from each of the four reconstructions to the Late Holocene baseline
505 SST. Due to nonlinear behavior of sea ice, the LGM and 2xCO₂ BCs for SIC are not added to the
506 baseline as anomalies but rather are used directly (Extended Data Fig. 2).

507 We run simulations with the Late Holocene baseline, 2xCO₂, and LGMR in each of five
508 AGCMs. We run simulations with all four of the LGM reconstructions (LGMR, lgmDA,
509 Amrhein, Annan) in CAM4 and CAM5, sampling the spread in LGM feedbacks from different
510 reconstructions in two AGCMs which, based on Green’s functions^{5,22}, have distinct relationships
511 linking SST patterns to their radiative feedbacks. Spin-up, analysis period, and year of
512 climatological forcing for each AGCM are 5yr/25yr/2000 (CESM1.2.2.1-CAM4⁶⁴,
513 CESM1.2.2.1-CAM5⁶⁵, and CESM2.1-CAM6⁶⁶ at 1.9° latitude x 2.5° longitude resolution);
514 5yr/25yr/2014 (HadGEM3-GC3.1-LL⁶⁷ at N96, approximately 135-km resolution) and
515 1yr/30yr/2001 (GFDL-AM4⁶⁸ at C96, approximately 100-km resolution). The parent coupled
516 models of the AGCMs considered here sample a wide range of climate sensitivities, from 2.95 K
517 (CAM4) to 5.54 K (HadGEM3-GC3.1-LL)²¹, and the AGCMs span a wide range of pattern
518 effects in the historical record, from 0.38 Wm⁻²K⁻¹ (HadGEM3-GC3.1-LL) to 0.84 Wm⁻²K⁻¹
519 (CAM6)²¹.

520 To compute λ , we take global means over the analysis periods for net top-of-atmosphere
521 radiative imbalance (N) and near-surface air temperature (T), also known as reference-height
522 temperature. Differences are taken relative to the Late Holocene baseline, yielding an “effective”

523 feedback⁶⁹ of $\lambda = \Delta N / \Delta T$ for LGM and 2xCO₂ simulations, given that $\Delta F = 0$ in equation (1) by
524 design.

525 To evaluate the impact of uncertainty in the 2xCO₂ pattern, we also consider existing
526 simulations of abrupt-4xCO₂ with 150-yr regressions⁷⁰ of ΔN versus ΔT , denoted as $\lambda_{4x(150yr)}$, to
527 estimate λ_{2x} (results in Ext. Data Figs. 3–4 and SI Tables 1–2). Results are consistent using either
528 method of estimating λ_{2x} . To compute $\Delta\lambda$ using $\lambda_{4x(150yr)}$, we apply a timescale adjustment (ζ) to
529 reconcile feedbacks from equilibrium paleoclimate data with the feedback that applies to 150-
530 year “effective” sensitivity (S), as in WCRP20. We use the central estimate from WCRP20 of
531 $\zeta = 0.06$, and equation (3) is modified to $\Delta\lambda = \lambda_{4x(150yr)} / (1 + \zeta) - \lambda_{LGM}$.

532 To investigate the effect of the most extreme ensemble members from the two most
533 recent LGM reconstructions on our results, we run additional simulations using CAM4 and
534 CAM5 with the quartiles of ensemble members that produce the most-negative and most-positive
535 λ_{LGM} in the LGMR¹⁰ and Annan¹² reconstructions (shown as error bars in Fig. 2). To determine
536 the SST/SIC boundary conditions for these experiments, the ensemble members in each dataset
537 are initially ranked by estimating λ_{LGM} , where λ_{LGM} is estimated by convolving the CAM5
538 Green’s functions²² with SST anomalies from each ensemble member. CAM4 Green’s functions⁵
539 produce similar rankings. Green’s functions are only used to rank ensemble members, and the
540 estimated feedbacks are not used thereafter. We group the ensemble members into quartiles
541 based on rank, and the mean SST/SIC (only SST for the Annan reconstruction) is computed
542 across ensemble members in each quartile. The SST anomalies representing the 1st and 4th
543 quartiles, i.e., the most-negative and least-negative feedbacks, are used in the additional AGCM
544 simulations (shown as error bars in Figure 2 and Extended Data Figure 3). Note that CAM5 with
545 the Annan ensemble’s extreme-negative λ_{LGM} produces $\Delta\lambda > 0$. In this quartile, most ensemble
546 members have warming at the LGM over substantial portions of the Southern Ocean (Extended
547 Data Fig. 10). This suggests that $\Delta\lambda$ could be positive if the Southern Ocean experienced
548 warming at the LGM, which is unlikely based on SST proxies^{2,10,71}, reconstructed deep-ocean
549 temperatures⁷² and proxy data indicating increased Antarctic sea ice at the LGM⁷³.

550

551 **Pattern-only simulations separating pattern and temperature dependence**

552 Feedback changes can be attributed to changes in SST patterns and changes in global-mean
553 temperature¹, such that $\Delta\lambda \approx \Delta\lambda_{\text{PatternOnly}} + \Delta\lambda_T$. To separate pattern and temperature impacts on

554 $\Delta\lambda$, we conduct additional “pattern-only” simulations in CAM4, CAM5, and CAM6 with the
 555 LGMR and 2xCO₂ patterns. For these simulations, we multiply local SST anomalies by constant
 556 scale factors, k , which are determined for each pattern so that the global-mean ΔSST is reduced
 557 to -0.5 K for both simulations. The constant scale factor for a given pattern of anomalies is
 558 calculated from the global-mean ΔSST as $k = \frac{-0.5 \text{ K}}{\Delta\text{SST}_{\text{global}}}$, and scaled patterns are then created as
 559 $\Delta\text{SST}_{\text{scaled}} = k\Delta\text{SST}$ at each gridcell. We hold SIC constant at the Late Holocene baseline.

560 SST scaling preserves the spatial pattern of anomalies but forces global-mean ΔT to be
 561 small enough that feedback changes due to temperature dependence are negligible ($\Delta\lambda_T \approx 0$). We
 562 repeat the feedback calculations, computing $\Delta\lambda_{\text{PatternOnly}} \approx \lambda_{2x}^{-0.5K} - \lambda_{\text{LGM}}^{-0.5K}$ as in equation (3).
 563 While there is no existing method that directly isolates temperature dependence in AGCM
 564 simulations, the temperature dependence can be approximated as the residual difference between
 565 our main and pattern-only simulations, rearranging equation (5) to $\Delta\lambda_T \approx \Delta\lambda - \Delta\lambda_{\text{PatternOnly}}$. In this
 566 framework, feedback changes due to sea ice are included in temperature dependence.

567 We employ this pattern-scaling method because it aligns with intuition for pattern effects
 568 captured by Green’s functions^{5,22,74}. We do not use Green’s functions to calculate the pattern-
 569 only feedbacks, but we briefly discuss the Green’s functions framework here to explain the
 570 pattern-only AGCM simulations. In that linear framework,

$$571 \quad \Delta N = \sum_j \frac{\partial N}{\partial \text{SST}_j} \Delta \text{SST}_j + \epsilon_N,$$

$$572 \quad \Delta T = \sum_j \frac{\partial T}{\partial \text{SST}_j} \Delta \text{SST}_j + \epsilon_T,$$

573 where j represents each gridcell, ΔSST_j represents the full SST anomaly at gridcell j , $\partial N/\partial\text{SST}_j$
 574 represents the global-mean top-of-atmosphere radiative response to a unit increase in local SST at
 575 gridcell j , $\partial T/\partial\text{SST}_j$ similarly represents the response of global-mean near-surface air temperature,
 576 and ϵ represents changes in N or T that are independent of SST. Because the feedback $\lambda = \Delta N/\Delta T$,
 577 constant scale factors, applied as $k\Delta\text{SST}$, appear in the feedback calculation as $\lambda = (k\Delta N)/(k\Delta T)$ if
 578 $\epsilon_N = \epsilon_T = 0$ and SST patterns determine λ . In this case where SST patterns are the sole control on
 579 λ , scale factors cancel and have no effect on feedbacks or pattern effects. By comparing feedbacks
 580 from scaled pattern-only simulations with feedbacks from simulations with full SST anomalies,
 581 we quantify feedback changes that cannot be explained by SST patterns, which we attribute to
 582 feedback dependence on global-mean temperature. For example, temperature dependence could

583 arise from $\frac{\partial N}{\partial SST_j}$ changing with global-mean temperature or from sea ice appearing at lower
584 latitudes as temperature decreases.

585 To examine whether results are sensitive to the scaling method of separating pattern effects
586 from temperature dependence, we tested an alternative subtraction method in CAM4 (using the
587 LGMR pattern for the LGM and the LongRunMIP pattern for 2xCO₂). We ran alternative pattern-
588 only simulations with global-mean SST anomalies set to zero by subtracting the global mean at all
589 locations. These experiments produced consistent results for $\Delta\lambda_{\text{PatternOnly}}$ compared to the scaling
590 method.

591

592 **Feedback decomposition using model fields and radiative kernels**

593 The net climate feedback (λ) is calculated from changes in net top-of-atmosphere radiation (ΔN)
594 divided by changes in global-mean temperature (ΔT). ΔN can be separated into shortwave clear-
595 sky (SWcs), longwave clear-sky (LWcs), and cloud radiative effect (CRE):

$$596 \quad \Delta N = \Delta N_{\text{SWcs}} + \Delta N_{\text{LWcs}} + \Delta N_{\text{CRE}},$$

597 where each component of the radiation is directly available from AGCM output, and dividing all
598 terms by ΔT yields feedbacks for each component which sum to the net feedback. The total
599 clear-sky feedback is the sum of shortwave and longwave components. These feedbacks are
600 plotted in Extended Data Figures 6–7. Because CRE is calculated as all-sky radiation (N) minus
601 clear-sky radiation, CRE is affected by changes in non-cloud variables, e.g., changes in sea ice
602 underneath clouds alter the CRE even when clouds are constant.

603 With radiative kernels^{75,76}, feedbacks can be decomposed into contributions from
604 temperature, moisture, and surface albedo. Cloud feedbacks can be more accurately isolated by
605 controlling for changes in non-cloud variables (cloud masking), which we do here following past
606 studies^{62,63}. Radiative kernels are linearized around a specific climate in a specific model,
607 however, and are prone to errors when applied to different climates and models. We use CAM5
608 kernels⁷⁷ in this study, convolving kernels with the monthly mean climatology of anomalies in
609 each AGCM simulation to produce component feedbacks shown in Extended Data Figures 6–7
610 and SI Section 5. HadGEM3-GC3.1-LL is not included in kernel analysis due to model-output
611 limitations. The GFDL-AM4 simulation of 2xCO₂ has error in the kernel-derived clear-sky
612 feedback equal to 15.6% of the actual clear-sky feedback, slightly exceeding the 15% threshold
613 commonly used as a test of clear-sky linearity^{9,75,78}; all other simulations have clear-sky feedback

614 errors less than 10%. Residuals shown in Extended Data Figure 6 are based on total (all-sky)
 615 radiation⁷⁸: $\lambda_{\text{Residual}} = \lambda_{\text{Net}} - \Sigma\lambda_j$, where λ_{Net} is the net feedback from model output, and $\Sigma\lambda_j$ is the
 616 sum of each of the following kernel-derived feedbacks: Planck, lapse rate, water vapor, surface
 617 albedo, shortwave cloud, and longwave cloud. We show the sum of $\lambda_{\text{LapseRate}}$ and $\lambda_{\text{WaterVapor}}$ as
 618 $\lambda_{\text{LR+WV}}$ given the anti-correlation of $\lambda_{\text{LapseRate}}$ and $\lambda_{\text{WaterVapor}}$ across models⁷⁹.

619

620 **Bayesian estimate of modern-day climate sensitivity**

621 We follow the WCRP20 method of calculating climate sensitivity¹. To clarify definitions,
 622 equilibrium climate sensitivity (ECS) is the steady-state change in global-mean temperature (T)
 623 from a doubling of CO₂, traditionally with ice sheets and vegetation assumed fixed. When
 624 inferring climate sensitivity that is relevant to modern warming from paleoclimate evidence,
 625 changes in the paleoclimate radiative budget that are distinct from feedback processes in a
 626 modern-day 2xCO₂ scenario are treated as forcings; this is typically accomplished by separating
 627 ‘slow’ timescale changes as forcings (e.g., ice sheets) from ‘fast’ timescale changes as feedbacks
 628 (e.g., clouds)¹⁵. WCRP20 applies this framework by focusing on the “effective” climate
 629 sensitivity (*S*), which is the sensitivity applicable to the 150-year system response. Using
 630 paleoclimate evidence to constrain modern-day *S* is a core concept in WCRP20, and we follow
 631 their methods here.

632 Relative to WCRP20, our key update affects only $\Delta\lambda$ for the LGM. However, given
 633 evidence^{2,3,10,49} published after WCRP20 showing LGM cooling centered around -6 °C instead
 634 of -5 °C, we report our main results using both values for ΔT_{LGM} (Fig. 4, Extended Data Fig. 4).

635 To estimate *S*, we use a modified version of WCRP20’s energy balance equation for the
 636 LGM,

$$637 \quad \Delta T_{\text{LGM}} = \frac{-(-0.57\Delta F_{2x} + \Delta F')}{\frac{\lambda_{2x}}{1+\zeta} - \Delta\lambda}, \quad (6)$$

638 which determines λ_{2x} and $S = -\Delta F_{2x}/\lambda_{2x}$. The modification substitutes our $\Delta\lambda$, which includes
 639 pattern and temperature dependence, for WCRP20’s $\Delta\lambda$. Other than testing a colder ΔT_{LGM} , the
 640 parameters are unchanged from WCRP20 and have the following Normal distributions: modern-
 641 day forcing from 2xCO₂ $\Delta F_{2x} \sim N(\mu=4.0, \sigma=0.3) \text{ Wm}^{-2}$; total non-CO₂ LGM forcing of $\Delta F' \sim$
 642 $N(-6.15, 2) \text{ Wm}^{-2}$ (consisting of -3.2 Wm^{-2} from ice sheets, -1.1 from vegetation, -1.0 from
 643 dust aerosols, -0.28 from N₂O, and -0.57 from CH₄); the timescale transfer parameter from
 644 paleoclimate ECS to the feedback for *S* on a 150-year timescale $\zeta \sim N(0.06, 0.2)$; and LGM

645 global-mean near-surface air temperature change $\Delta T_{\text{LGM}} \sim N(-5, 1)$ °C, or with revised $\Delta T_{\text{LGM}} \sim$
646 $N(-6, 1)$ °C based on recent evidence^{2,3,10,49} post WCRP20. In WCRP20, $\Delta\lambda = \Delta\lambda_{\text{T}} = -\alpha\Delta T_{\text{LGM}}/2$,
647 with $\alpha \sim N(\mu = 0.1, \sigma = 0.1)$ $\text{Wm}^{-2}\text{K}^{-2}$. We note that treatment and quantification of non-CO₂
648 effective radiative forcing from ice sheets (including sea level), dust aerosols, vegetation, and
649 other greenhouse gases represents substantial uncertainty. As noted in ref.²⁶, estimates of the
650 effective radiative forcing (ERF) for each component of non-CO₂ LGM forcing still need to be
651 constrained. Recent assessments¹⁻³ discuss how dust aerosols^{80,81}, vegetation, and non-CO₂
652 greenhouse gases also act as feedbacks on fast timescales, hence ref.² shows multiple options for
653 calculating LGM sensitivity. IPCC AR6³ presents these biogeophysical and non-CO₂
654 biogeochemical changes as feedbacks (with a combined central value of $-0.01 \text{ Wm}^{-2}\text{K}^{-1}$) in their
655 framework for modern-day ECS, but AR6 does not address how to account for the LGM's
656 distinct non-CO₂ changes (other than ice sheets) in a modern-day 2xCO₂ scenario.

657 From the AGCM results in this study, we incorporate pattern effects in $\Delta\lambda$ of equation
658 (6), assigning a revised $\Delta\lambda \sim N(-0.37, 0.23)$ $\text{Wm}^{-2}\text{K}^{-1}$. The revised distribution for $\Delta\lambda$ in our
659 study is based on propagating uncertainty, estimated as spread across AGCMs and LGM
660 reconstructions. To combine uncertainty, we assume that within CAM6, GFDL-AM4, and
661 HadGEM3, the spread in $\Delta\lambda$ from different LGM reconstructions would be the same as the
662 spread in $\Delta\lambda$ from different LGM reconstructions within CAM4 and CAM5. We add the
663 differences in $\Delta\lambda$ from each pattern in CAM4 and CAM5, where differences are computed
664 relative to the LGMR result for $\Delta\lambda$, to the LGMR results from the remaining three AGCMs. The
665 effect is to treat errors as arising independently in reconstructions and AGCMs. We include $\Delta\lambda$
666 from extreme-quartile simulations using ensemble members from Annan and LGMR in the
667 combined sample; i.e., there are 8 simulations from CAM4 and 8 simulations from CAM5 that
668 determine the spread from LGM patterns. Note that the spread from LGM patterns is similar
669 between CAM4 and CAM5 (Fig. 2).

670 From the combined uncertainty estimates, we perform bootstrap sampling (described in
671 SI Section 4) with 10^5 iterations and a sample size of 19 (equal to the number of actual AGCM
672 simulations). The mean over all bootstrap iterations is $\overline{\Delta\lambda} = -0.37$ (95% CI: -0.47 to -0.26)
673 $\text{Wm}^{-2}\text{K}^{-1}$, which informs μ in our assigned distribution, and mean sample standard deviation =
674 0.23 (95% range: 0.15 to 0.31) $\text{Wm}^{-2}\text{K}^{-1}$, which informs σ in our assigned distribution. In
675 Extended Data Figure 4, we include an uncertainty test by doubling the standard deviation to $\sigma =$

676 $0.46 \text{ Wm}^{-2}\text{K}^{-1}$, which significantly exceeds the upper bound on the 95% range from the
677 bootstrap estimate. To determine the distribution of $\Delta\lambda$ in Extended Data Figure 4, we repeat the
678 bootstrap estimate using $\lambda_{4x(150\text{yr})}/1.06$ instead of λ_{2x} , where 1.06 represents WCRP20's central
679 estimate¹ for the timescale adjustment between the 150-year feedback and the equilibrium
680 feedback; this yields $\overline{\Delta\lambda} = -0.27 \text{ Wm}^{-2}\text{K}^{-1}$ and mean sample standard deviation = 0.20
681 $\text{Wm}^{-2}\text{K}^{-1}$. Note that our method of combining uncertainty gives equal weight to the most-
682 extreme quartiles and to the central estimates, but this overestimate of uncertainty is warranted
683 given that paleoclimate data assimilation may underestimate the true uncertainty³⁵. The
684 uncertainty estimate also gives more weight to the most recent reconstructions, LGMR¹⁰ and
685 Annan¹², by including three simulations (mean, 1st quartile, and 4th quartile) from these datasets.
686 The weighting influences the bootstrap estimate and the distribution assigned to $\Delta\lambda$ in our
687 calculations of ECS.

688 Over the range of temperatures between the LGM and 2xCO₂, all five AGCMs appear to
689 have weaker temperature dependence of feedbacks than WCRP20 assumes, i.e., $\Delta\lambda_T$ appears
690 smaller than in WCRP20. $\Delta\lambda_T$ could be underestimated in all models, so we include an
691 uncertainty test where we use the pattern-only simulations in CAM4, CAM5, and CAM6 to
692 estimate the mean $\Delta\lambda_{\text{PatternOnly}}$ contribution to the total $\Delta\lambda$, and we retain WCRP20's estimate of
693 $\Delta\lambda_T$. In this uncertainty test, $\Delta\lambda$ in equation (6) is calculated as the sum of $\Delta\lambda_T$ and $\Delta\lambda_{\text{PatternOnly}}$:
694 $\Delta\lambda_T = -\alpha\Delta T/2$ with $\alpha \sim N(0.1, 0.1) \text{ Wm}^{-2}\text{K}^{-2}$ as in WCRP20, while $\Delta\lambda_{\text{PatternOnly}} \sim N(-0.51, 0.23)$
695 $\text{Wm}^{-2}\text{K}^{-1}$ with μ based on CAM4, CAM5, and CAM6 results (SI Table 3). The results of this
696 uncertainty test are included in Extended Data Figure 9, indicating that accounting for pattern
697 effects causes the dominant change to LGM evidence for ECS, while the revision to WCRP20's
698 temperature dependence contributes a smaller portion of the update.

699 The LGM likelihood is computed using Monte Carlo sampling for all parameters, as in
700 WCRP20. For each random draw j , the likelihood is the probability density evaluated at the
701 observational estimate of $\Delta T_{\text{LGM}} = -5 \text{ K}$ (or revised $\Delta T_{\text{LGM}} = -6 \text{ K}$) from the distribution $N(\Delta T_j,$
702 $1) \text{ K}$, where ΔT_j is produced by the j^{th} random draw of parameters in equation (6). The resulting
703 probability densities form the likelihood functions for $S = -\Delta F_{2x}/\lambda_{2x}$. The likelihood functions
704 can be visualized as histograms where the individual likelihoods for each random draw of
705 parameters become the probability weights associated with each value of λ_{2x} and S . We show the
706 likelihood functions using kernel density estimation, following methods in WCRP20.

707 The likelihood functions are independent of the choice of prior, but combining the
708 likelihoods and prior is required to create posterior PDFs for the combined lines of evidence. We
709 follow methods¹ and code⁸² provided by WCRP20 to update the combined-evidence posterior
710 PDF for both the Uniform(0, 20) °C prior on S and the Uniform(-10, 10) Wm⁻²K⁻¹ prior on λ .
711 WCRP20 uses the uniform- λ prior as their “Baseline,” although the uniform-S prior may be
712 preferable because it is more conservative regarding the possibility of high climate sensitivity.
713 We show results from both priors in the main text. For clarity, our combined-evidence posterior
714 PDFs are identical to those in WCRP20, including their process-understanding, historical, and
715 paleoclimate warm-period evidence, with the only change being $\Delta\lambda$ for the LGM (the
716 paleoclimate cold-period evidence).

717

718

719 **Methods References**

- 720 51. Parsons, L. A. *et al.* Do Multi-Model Ensembles Improve Reconstruction Skill in Paleoclimate Data
721 Assimilation? *Earth and Space Science* **8**, e2020EA001467 (2021).
- 722 52. Waelbroeck, C. *et al.* Constraints on the magnitude and patterns of ocean cooling at the Last Glacial
723 Maximum. *Nature Geoscience* **2**, 127–132 (2009).
- 724 53. Brady, E. C., Otto-Bliesner, B. L., Kay, J. E. & Rosenbloom, N. Sensitivity to Glacial Forcing in the
725 CCSM4. *J Clim* **26**, 1901–1925 (2013).
- 726 54. Peltier, W. R., Argus, D. F. & Drummond, R. Space geodesy constrains ice age terminal deglaciation:
727 The global ICE-6G-C (VM5a) model. *J Geophys Res Solid Earth* **120**, (2015).
- 728 55. Argus, D. F., Peltier, W. R., Drummond, R. & Moore, A. W. The Antarctica component of postglacial
729 rebound model ICE-6G_C (VM5a) based on GPS positioning, exposure age dating of ice thicknesses,
730 and relative sea level histories. *Geophys J Int* **198**, (2014).
- 731 56. DiNezio, P. N. & Tierney, J. E. The effect of sea level on glacial Indo-Pacific climate. *Nat Geosci* **6**,
732 485–491 (2013).
- 733 57. Gent, P. R. *et al.* The Community Climate System Model Version 4. *J Clim* **24**, 4973–4991 (2011).
- 734 58. Voldoire, A. *et al.* Evaluation of CMIP6 DECK Experiments With CNRM-CM6-1. *J Adv Model*
735 *Earth Syst* **11**, 2177–2213 (2019).
- 736 59. Cox, P. M., Betts, R. A., Jones, C. D., Spall, S. A. & Totterdell, I. J. Acceleration of global warming
737 due to carbon-cycle feedbacks in a coupled climate model. *Nature* **408**, 184–187 (2000).
- 738 60. Mauritsen, T. *et al.* Developments in the MPI-M Earth System Model version 1.2 (MPI-ESM1.2) and
739 Its Response to Increasing CO₂ Developments in the MPI-M Earth System Model version 1.2 (MPI-
740 ESM1.2) and its response to increasing CO₂ Journal of Advances in Modeling Earth Systems. *J Adv*
741 *Model Earth Syst* **11** (2019) doi:10.1029/2018MS001400.
- 742 61. Paynter, D., Frölicher, T. L., Horowitz, L. W. & Silvers, L. G. Equilibrium Climate Sensitivity
743 Obtained From Multimillennial Runs of Two GFDL Climate Models. *Journal of Geophysical*
744 *Research: Atmospheres* **123**, 1921–1941 (2018).
- 745 62. K-1 Model Developers. *K-1 Coupled GCM (MIROC) Description*. (2004).
- 746 63. Yamamoto, A. *et al.* Global deep ocean oxygenation by enhanced ventilation in the Southern Ocean
747 under long-term global warming. *Global Biogeochem Cycles* **29**, 1801–1815 (2015).
- 748 64. Neale, R. B. *et al.* The Mean Climate of the Community Atmosphere Model (CAM4) in Forced SST
749 and Fully Coupled Experiments. *J Clim* **26**, 5150–5168 (2013).
- 750 65. Neale, R. B. *et al.* *Description of the NCAR Community Atmosphere Model (CAM 5.0) (NCAR/TN-*
751 *486+STR)*. (2012) doi:http://dx.doi.org/10.5065/wgtk-4g06.
- 752 66. Danabasoglu, G. *et al.* The Community Earth System Model Version 2 (CESM2). *J Adv Model Earth*
753 *Syst* **12**, (2020).
- 754 67. Williams, K. D. *et al.* The Met Office Global Coupled Model 3.0 and 3.1 (GC3.0 and GC3.1)
755 Configurations. *J Adv Model Earth Syst* **10**, 357–380 (2017).
- 756 68. Held, I. M. *et al.* Structure and Performance of GFDL’s CM4.0 Climate Model. *J Adv Model Earth*
757 *Syst* **11**, 3691–3727 (2019).
- 758 69. Rugenstein, M. A. A. & Armour, K. C. Three Flavors of Radiative Feedbacks and Their Implications
759 for Estimating Equilibrium Climate Sensitivity. *Geophys Res Lett* **48**, (2021).
- 760 70. Gregory, J. M. A new method for diagnosing radiative forcing and climate sensitivity. *Geophys Res*
761 *Lett* **31**, L03205 (2004).
- 762 71. Waelbroeck, C. *et al.* Constraints on the magnitude and patterns of ocean cooling at the Last Glacial
763 Maximum. *Nature Geoscience* **2**, 127–132 (2009).
- 764 72. Adkins, J. F., McIntyre, K. & Schrag, D. P. The Salinity, Temperature, and $\delta^{18}\text{O}$ of the Glacial Deep
765 Ocean. *Science* (1979) **298**, 1769–1773 (2002).
- 766 73. Green, R. A. *et al.* Evaluating seasonal sea-ice cover over the Southern Ocean at the Last Glacial
767 Maximum. *Climate of the Past* **18**, 845–862 (2022).

- 768 74. Zhang, B., Zhao, M. & Tan, Z. Using a Green's Function Approach to Diagnose the Pattern Effect in
769 GFDL AM4 and CM4. *J Clim* **36**, 1105–1124 (2023).
- 770 75. Shell, K. M., Kiehl, J. T. & Shields, C. A. Using the Radiative Kernel Technique to Calculate Climate
771 Feedbacks in NCAR's Community Atmospheric Model. *J Clim* **21**, 2269–2282 (2008).
- 772 76. Soden, B. J. *et al.* Quantifying Climate Feedbacks Using Radiative Kernels. *J Clim* **21**, 3504–3520
773 (2008).
- 774 77. Pendergrass, A. G., Conley, A. & Vitt, F. M. Surface and top-of-atmosphere radiative feedback
775 kernels for CESM-CAM5. *Earth Syst. Sci. Data* **10**, 317–324 (2018).
- 776 78. Zelinka, M. D. *et al.* Causes of Higher Climate Sensitivity in CMIP6 Models. *Geophys Res Lett* **47**,
777 (2020).
- 778 79. Soden, B. J. & Held, I. M. An Assessment of Climate Feedbacks in Coupled Ocean–Atmosphere
779 Models. *J Clim* **19**, 3354–3360 (2006).
- 780 80. Sagoo, N. & Storelvmo, T. Testing the sensitivity of past climates to the indirect effects of dust.
781 *Geophys Res Lett* **44**, 5807–5817 (2017).
- 782 81. Albani, S. *et al.* Aerosol–Climate Interactions During the Last Glacial Maximum. *Curr Clim Change*
783 *Rep* **4**, 99–114 (2018).
- 784 82. Webb, M. *Code and Data for WCRP Climate Sensitivity Assessment*. Zenodo (2020)
785 doi:10.5281/zenodo.3945275.
- 786 83. Computational and Information Systems Laboratory. Cheyenne: HPE/SGI ICE XA System
787 (University Community Computing). Preprint at <https://doi.org/10.5065/D6RX99HX> (2019).
- 788 84. Pendergrass, A. G. *CAM5 Radiative Kernels [Data set]*. (2017) doi:doi.org/10.5065/D6F47MT6.
- 789 85. Pendergrass, A. G. *apendergrass/cam5-kernels: Up to date codebase as of August 2019*. (2019)
790 doi:doi.org/10.5281/zenodo.3359041.

791
792
793
794 **Acknowledgments** V.T.C. acknowledges funding from the NDSEG Fellowship (USA Dept. of
795 Defense) and NCAR/CISL/Cheyenne computing resources⁸³. V.T.C., K.C.A., and G.J.H.
796 acknowledge funding from National Science Foundation (NSF) Award OCE-2002276; C.P. from
797 NSF OCE-2002385; N.J.B. from NSF OCE-2002448 and AGS-1844380; J.E.T. and M.B.O.
798 from NSF OCE-2002398. K.C.A. acknowledges funding from the National Oceanic and
799 Atmospheric Administration (NOAA) MAPP Program Award NA20OAR4310391 and an Alfred
800 P. Sloan Research Fellowship (Grant FG-2020-13568). Y.D. was supported by the NOAA
801 Climate and Global Change Postdoctoral Fellowship Program, administered by UCAR's
802 Cooperative Programs for the Advancement of Earth System Science (CPAESS) under award
803 NA210AR4310383. T.A. was supported by the Met Office Hadley Centre Climate Programme
804 funded by BEIS and received funding from the European Union's Horizon 2020 research and
805 innovation programme under grant agreement 820829. The CESM project is supported primarily
806 by the NSF. This material is based upon work supported by the National Center for Atmospheric
807 Research, which is a major facility sponsored by the NSF under Cooperative Agreement No.
808 1852977.

809 **Author contributions** V.T.C. performed the analysis, designed the simulations, wrote the paper,
810 and ran the simulations in CAM5 and CAM4; K.C.A. initiated the study with support from
811 G.J.H., C.P., J.E.T, and N.J.B; K.C.A. and G.J.H. supervised the research; G.J.H., J.E.T.,
812 M.B.O., and D.E.A. contributed expertise on data assimilation and LGM reconstructions; Y.D.,
813 N.J.B., T.A., C.P., J.Z., and Y.M. contributed to analysis and interpreting results; T.A. ran
814 AGCM simulations in HadGEM3-GC3.1-LL, W.D. in GFDL-AM4, and P.C. in CAM6; J.Z.
815 provided coupled simulations in CESM; all authors contributed to editing the paper.

816

817 **Competing interests** The authors declare no competing interests.

818

819 **Data availability** AGCM results and SST/SIC boundary conditions are available at
820 github.com/vtcooper/cooper_etal_2023_LGMpattern. LongRunMIP is available at
821 longrunmip.org, LGMR¹⁰ at doi.org/10.25921/njxd-hg08, lgmDA² v2.1 at
822 doi.org/10.5281/zenodo.5171432, Amrhein¹¹ at doi.org/10.5281/zenodo.8110710, and Annan¹²
823 in the supplement of doi.org/10.5194/cp-18-1883-2022. Coupled-model simulations from
824 previous studies of the LGM are available at doi.org/10.5281/zenodo.3948405 (CESM1-
825 CAM5)²⁶, doi.org/10.5281/zenodo.4075596 (CESM2-CAM6)⁴³, and doi.org/10.5065/bdr7-wt42
826 (CESM2-PaleoCalibr)⁴⁴.

827

828 **Code availability** CESM1.2.2.1 is publicly available at [svn-ccsm-](https://svn-ccsm-models.cgd.ucar.edu/cesm1/release_tags/cesm1_2_2_1/)
829 [models.cgd.ucar.edu/cesm1/release_tags/cesm1_2_2_1/](https://svn-ccsm-models.cgd.ucar.edu/cesm1/release_tags/cesm1_2_2_1/) (including CAM4 and CAM5).
830 CESM2.1.3 (CAM6) is publicly available at github.com/ESCOMP/CESM. GFDL-AM4 is
831 publicly available at data1.gfdl.noaa.gov/nomads/forms/am4.0/. Code from WCRP20 to compute
832 climate sensitivity with Bayesian methods for combining lines of evidence⁸² is available at
833 doi.org/10.5281/zenodo.3945276. CAM5 radiative kernels⁷⁷ are available at
834 doi.org/10.5065/D6F47MT6 (dataset)⁸⁴ and doi.org/10.5281/zenodo.997899 (software)⁸⁵.

835

836 **Corresponding author** Vince Cooper (vcooper@uw.edu)

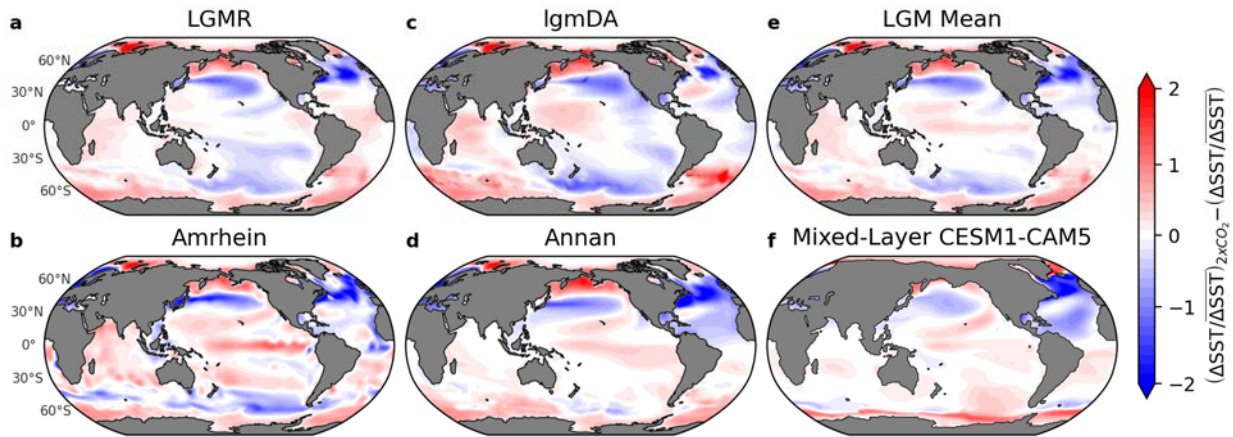
837

838 **Extended Data**

839

840

841



842

843

844 **Extended Data Fig. 1 | Differences in LGM sea-surface temperature (SST) patterns**

845 **compared to 2xCO₂ reference pattern.** All local anomalies are normalized through division by

846 global-mean anomaly, then differences between the 2xCO₂ pattern and LGM pattern are taken.

847 Red regions indicate where SST anomalies are relatively more amplified in 2xCO₂, while blue

848 regions indicate where SST anomalies are relatively more amplified at the LGM. **a-e**, LGM

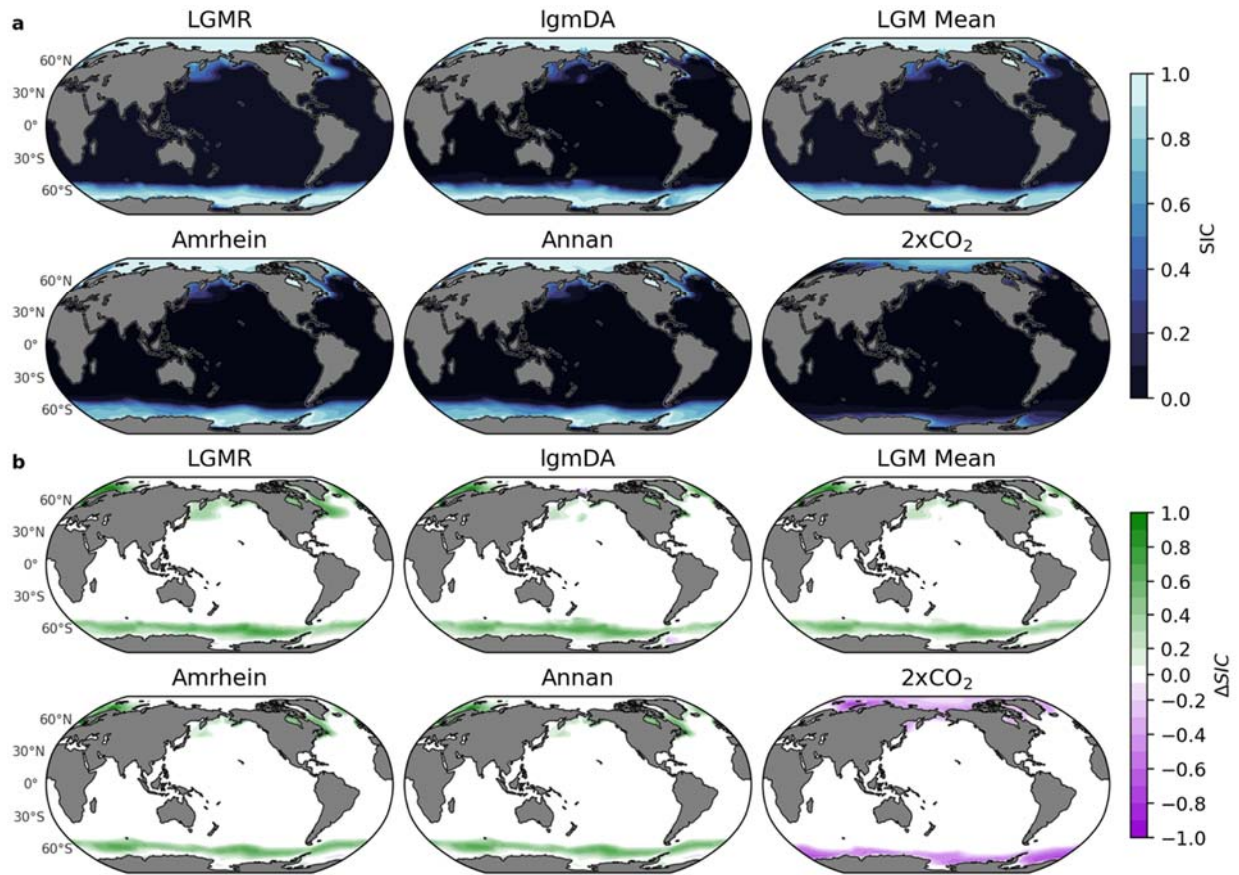
849 patterns corresponding to Fig. 1a-e, and 2xCO₂ reference pattern is Fig. 1f from LongRunMIP-

850 2xCO₂. **f**, In CESM1-CAM5²⁶ mixed-layer ocean model without data assimilation, difference

851 between 2xCO₂ and LGM patterns (shown in Extended Data Figure 5c-d).

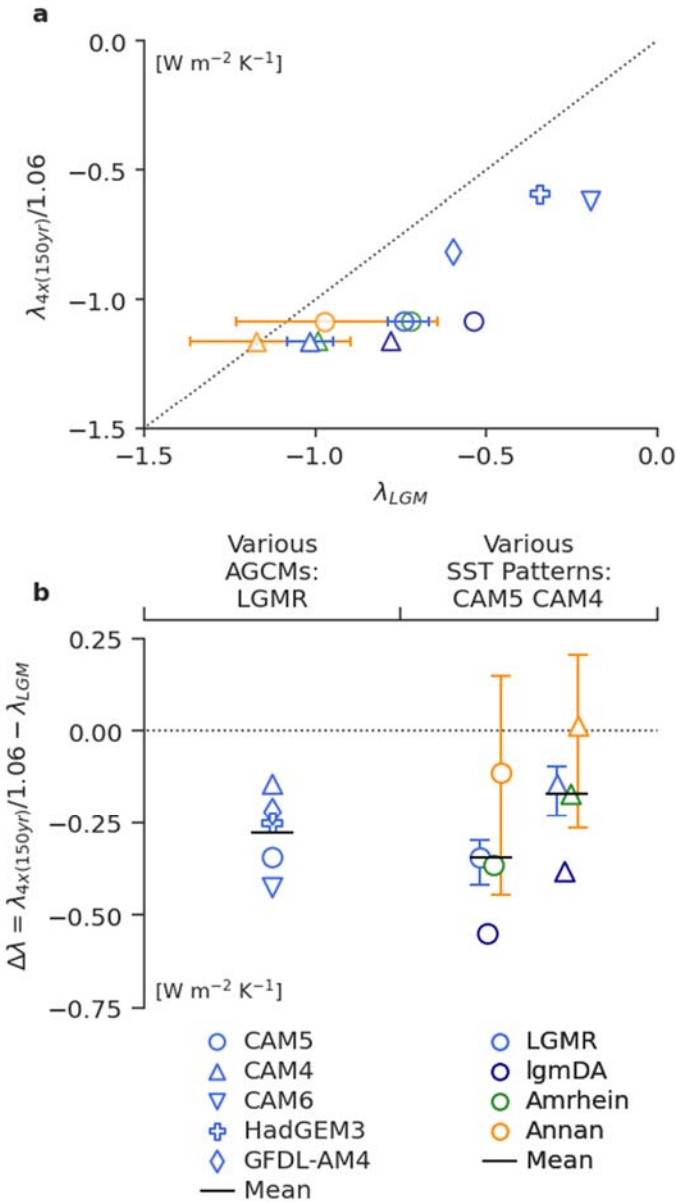
852

853

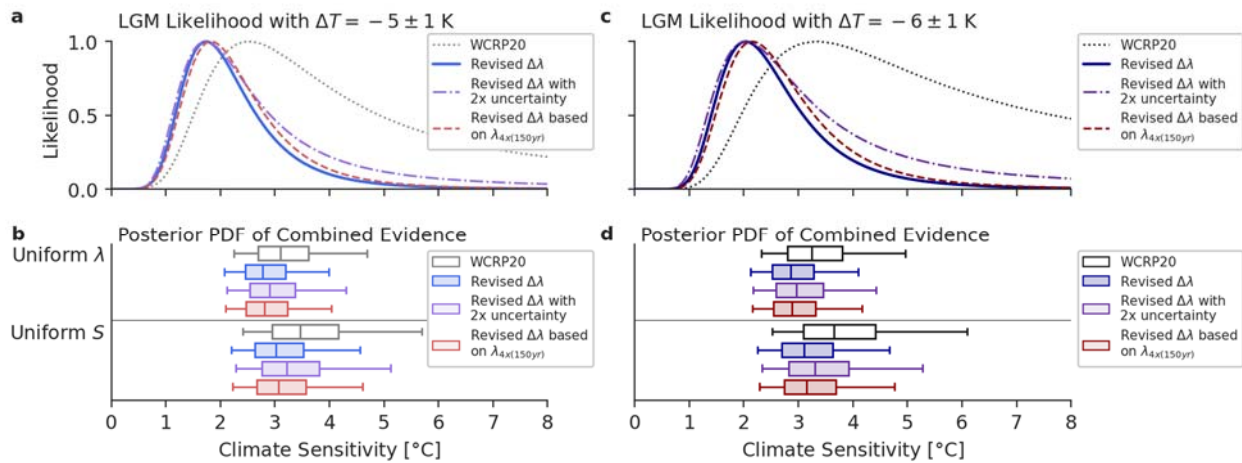


854
 855
 856
 857
 858
 859
 860
 861
 862
 863
 864
 865

Extended Data Fig. 2 | Sea-ice concentration (SIC) from data-assimilation reconstructions of the Last Glacial Maximum (LGM) compared to 2xCO₂. **a**, SIC from LGM Reanalysis (LGMR)¹⁰, Amrhein¹¹, lgmDA², Annan¹² (assigned SIC from Amrhein); mean of three LGM reconstructions (LGMR, Amrhein, and lgmDA); and multi-model mean from near-equilibrium simulations of 2xCO₂ in LongRunMIP³⁴, where each of six models is averaged over final 200 years of simulation. **b**, Difference in sea-ice concentration relative to Late Holocene baseline (LGMR reconstruction). All panels show annual mean. Reconstructions are infilled to modern coastlines (Methods).



866
 867 **Extended Data Fig. 3 | Last Glacial Maximum (LGM) pattern effect ($\Delta\lambda$) based on LGM**
 868 **climate feedbacks in AGCMs and CO₂ climate feedbacks from 150-yr regression of abrupt-**
 869 **4xCO₂ in coupled models.** Identical to Fig. 2, except λ_{2x} is replaced by $\lambda_{4x(150yr)}/1.06$, the
 870 feedback from regression in abrupt-4xCO₂ simulations⁷⁰ using parent coupled models
 871 corresponding to each AGCM; a timescale adjustment¹ of 1/1.06 is applied (based on WCRP20
 872 central estimate¹) to make 150-year 4xCO₂ feedbacks comparable with λ_{LGM} equilibrium
 873 feedbacks. Different models (all using the LGMR pattern for the LGM) are indicated by
 874 symbols. Different LGM patterns (in CAM5 and CAM4) are indicated by colors. **a**, Scatter plot
 875 of 4xCO₂ feedbacks (including adjustment factor of 1/1.06) versus LGM feedbacks, with
 876 $\lambda_{4x(150yr)}/1.06 = \lambda_{LGM}$ shown as dashed line. **b**, LGM pattern effect, $\Delta\lambda = \lambda_{4x(150yr)}/1.06 - \lambda_{LGM}$, using
 877 feedbacks shown in panel **a**, with $\Delta\lambda = 0$ shown as dashed line.



879

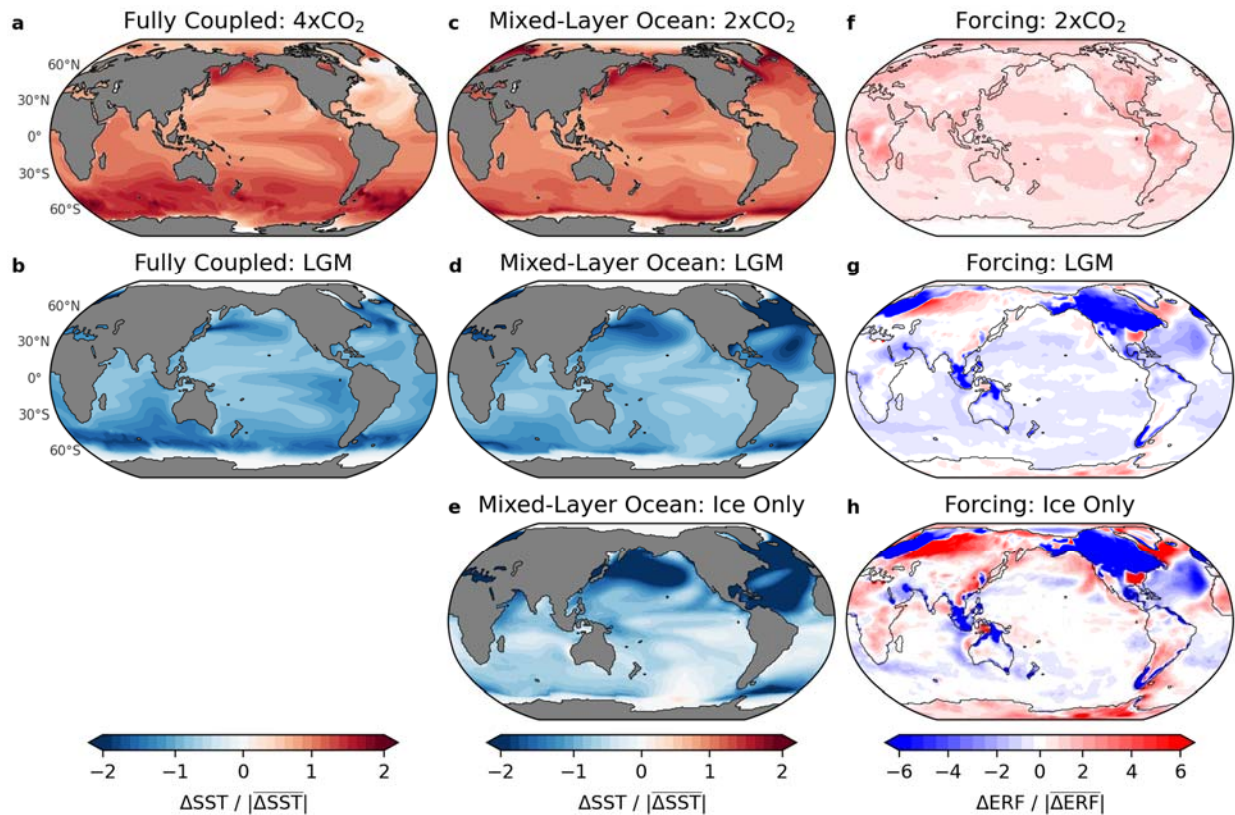
880

881 **Extended Data Fig. 4 | Uncertainty tests for modern-day climate sensitivity including the**
 882 **LGM pattern effect.** Following Fig. 4, showing WCRP20 original¹ LGM $\Delta T_{\text{LGM}} \sim N(\mu=-5, \sigma=1)$ K in left column and revised LGM $\Delta T_{\text{LGM}} \sim N(\mu=-6, \sigma=1)$ K based on IPCC AR6³ in right
 883 column, including two uncertainty tests. Results from WCRP20¹ with no LGM pattern effect
 884 (gray and black) and our base assumption (light and dark blue) for revised $\Delta\lambda \sim N(-0.37, 0.23)$
 885 $\text{Wm}^{-2}\text{K}^{-1}$ from Fig. 4 are repeated here for comparison. First uncertainty test (light and dark
 886 purple) increases the σ assumption by a factor of two: $\Delta\lambda \sim N(-0.37, 0.46)$ $\text{Wm}^{-2}\text{K}^{-1}$. Second
 887 uncertainty test (light and dark red) concerns the 2xCO₂ pattern and feedback: a different
 888 distribution, $\Delta\lambda \sim N(-0.27, 0.20)$ $\text{Wm}^{-2}\text{K}^{-1}$, is assigned based on results shown in Ext. Data Fig. 3
 889 using $\lambda_{4x(150\text{yr})}/1.06$, the feedback derived from 150-year regressions⁷⁰ of abrupt-4xCO₂ using
 890 parent coupled models corresponding to each AGCM, including a timescale-adjustment factor¹
 891 of 1/1.06 (WCRP20's central estimate¹). Climate sensitivity shown is effective sensitivity (S)
 892 from 150-year response, as in WCRP20¹. **a**, Likelihood functions for S based on only the LGM
 893 line of evidence. **b**, Posterior PDF after combining LGM with other lines of evidence in
 894 WCRP20¹, assuming a uniform- λ prior (upper panel) or a uniform- S prior (lower panel). Outlier
 895 lines indicate 5–95th percentiles, and box indicates 25–75th percentiles and median.

897

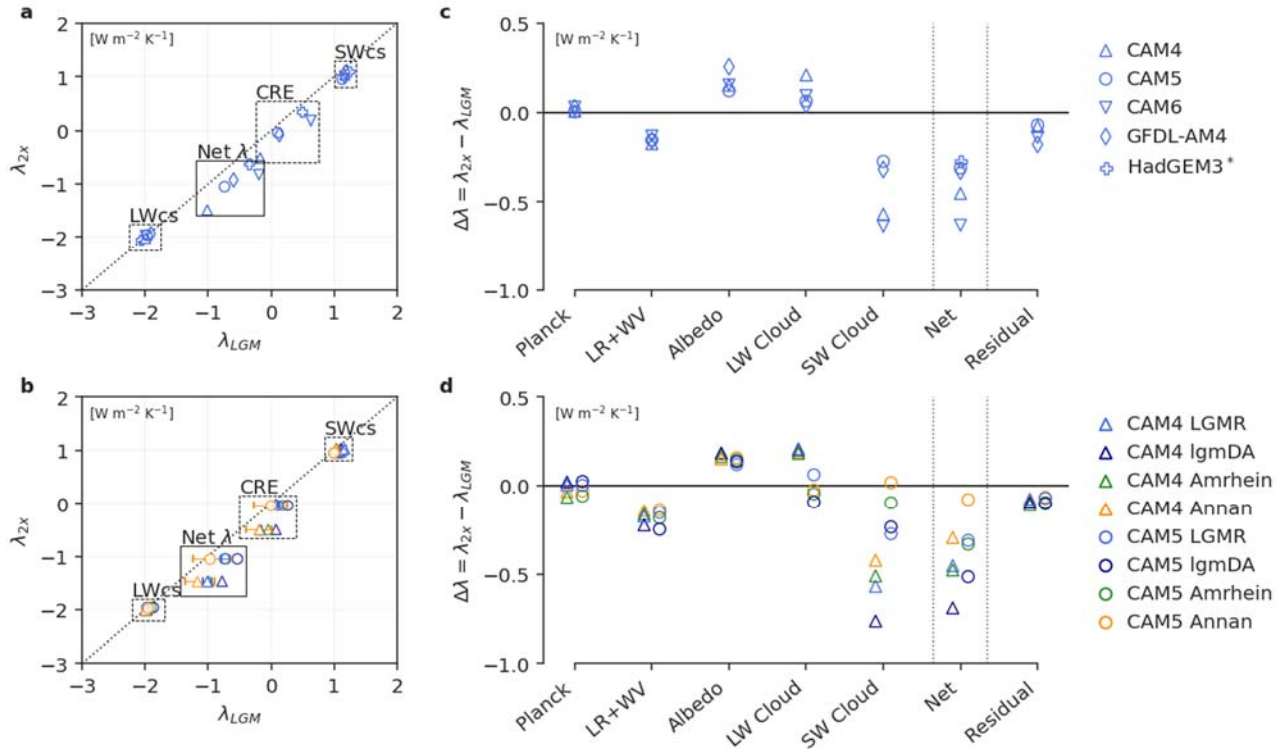
898

899

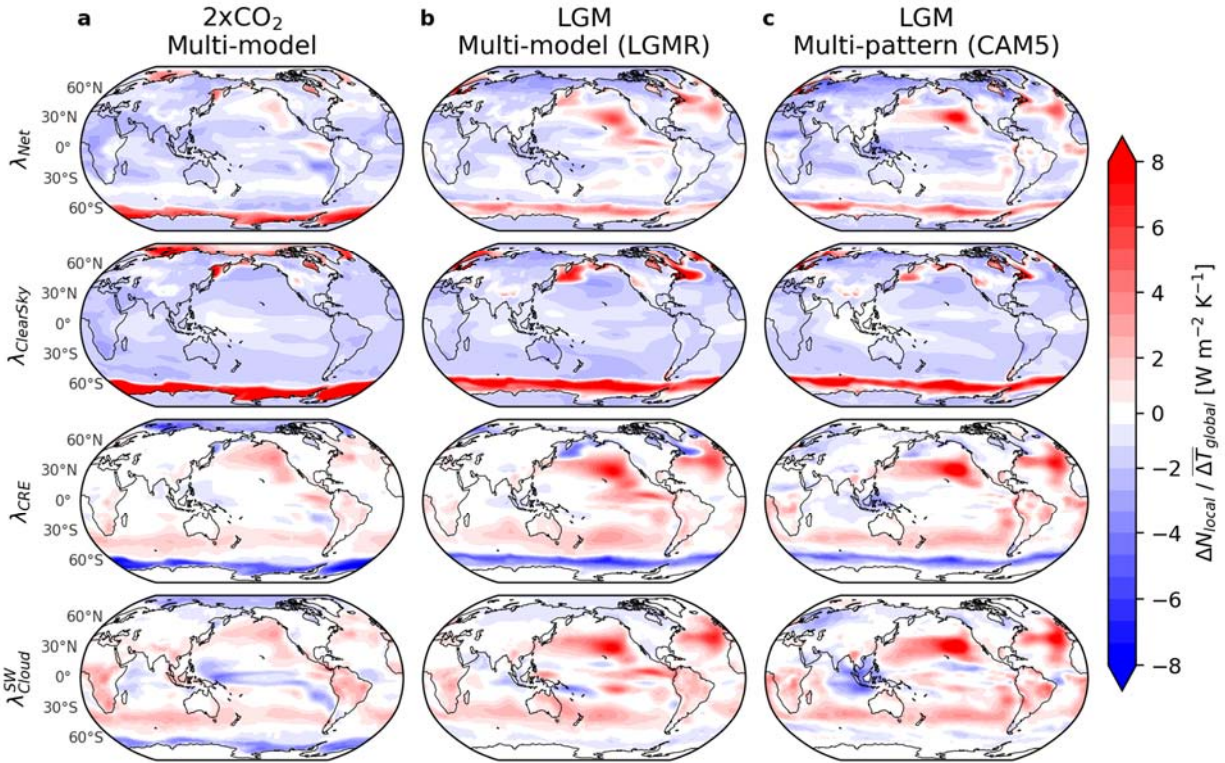


900
 901
 902
 903
 904
 905
 906
 907
 908
 909
 910
 911

Extended Data Fig. 5 | Spatial patterns of sea-surface temperature (SST) response and effective radiative forcing (ERF) in CESM1-CAM5 model simulations from Zhu & Poulsen²⁶. Spatial patterns here are shown as zonal means in Fig. 2. All local anomalies are normalized through division by absolute value of global-mean anomaly. **a–b**, SST patterns in quasi-equilibrium from fully coupled atmosphere-ocean model with LGM ice-sheet and GHG forcings²⁶ compared to abrupt-4xCO₂ forcing⁴⁶. **c–e**, Equilibrium SST patterns from mixed-layer ocean model coupled to CAM5, including a simulation with only LGM ice-sheet forcing²⁶. **f–h**, ERF patterns from corresponding AGCM simulations in CAM5.



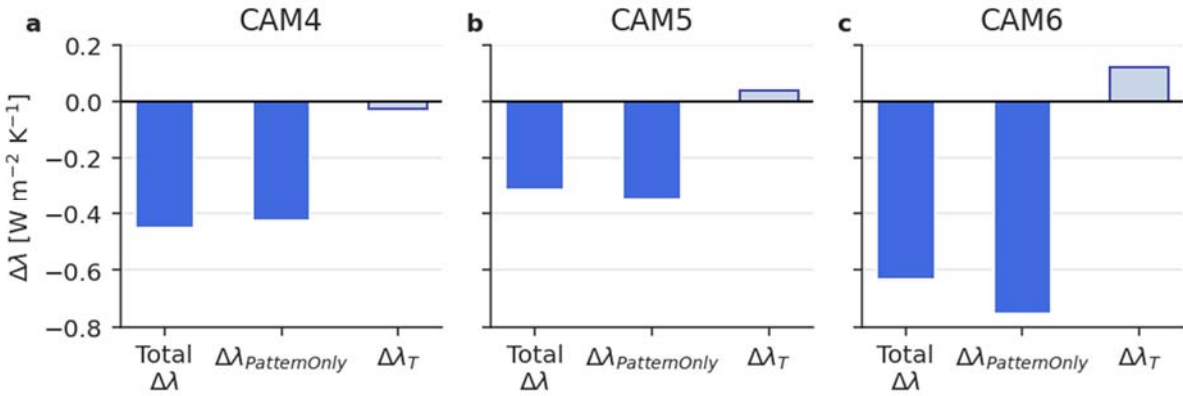
912
 913 **Extended Data Fig. 6 | Feedback decomposition of Last Glacial Maximum (LGM) and**
 914 **2xCO₂ climate feedbacks in atmospheric general circulation models (AGCMs).** Left column
 915 uses direct model outputs in scatter plots of 2xCO₂ feedbacks (λ_{2x}) versus LGM feedbacks
 916 (λ_{LGM}), with $\lambda_{2x}=\lambda_{LGM}$ denoted by dashed line. Cloud radiative effect (CRE), shortwave clear-sky
 917 (SWcs), longwave clear-sky (LWcs), and net feedbacks are shown. **a**, Results from various
 918 AGCMs, all using the LGMR reconstruction for the LGM. **b**, Results from various LGM
 919 reconstructions in CAM4 and CAM5, with different reconstructions indicated by colors. Right
 920 column shows decomposition of $\Delta\lambda$ using CAM5 radiative kernels⁷⁷, with residual equal to the
 921 net feedback in models minus the sum of kernel-derived feedbacks. **c**, Results from various
 922 AGCMs (note that only net λ is available for HadGEM3). **d**, Results from various LGM
 923 reconstructions in CAM4 and CAM5.
 924



925
926

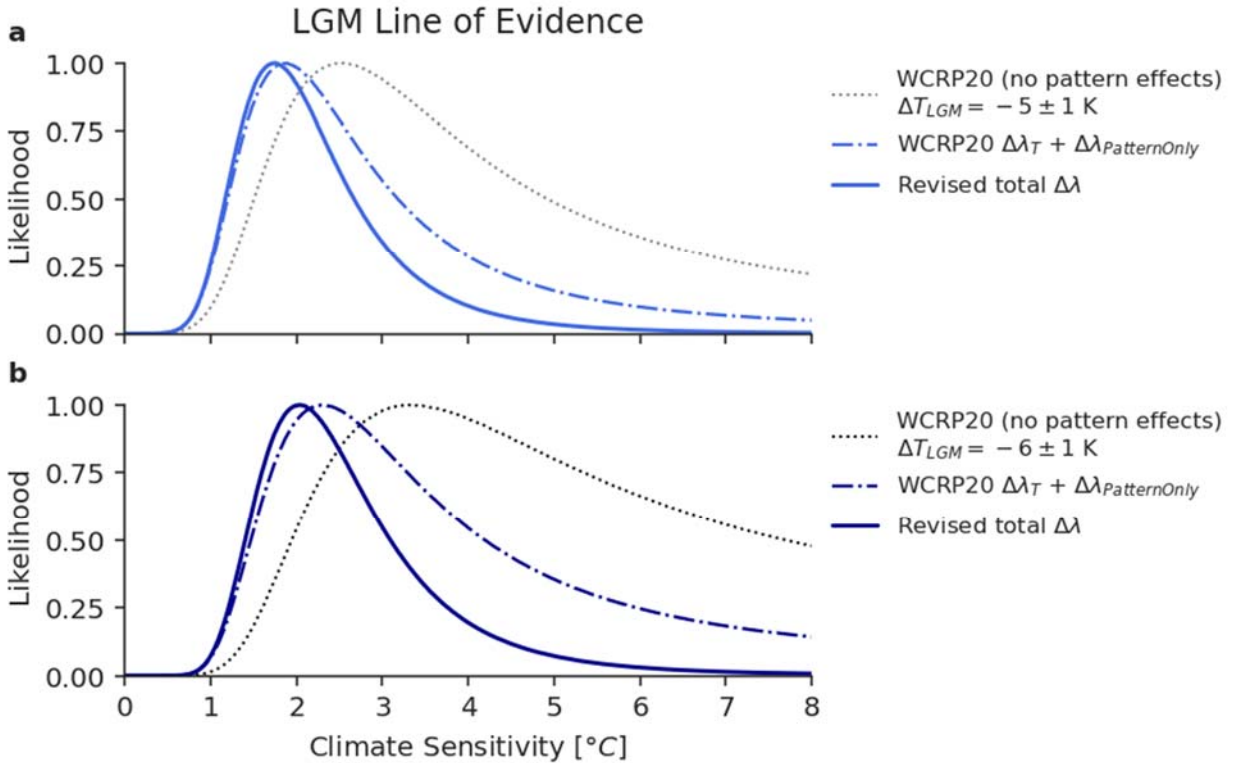
927 **Extended Data Fig. 7 | Spatial decomposition of Last Glacial Maximum (LGM) and 2xCO₂**
 928 **local climate feedbacks in atmospheric general circulation models (AGCMs).** Local
 929 feedbacks represent local change in top-of-atmosphere radiation (ΔN_{local}) divided by global-mean
 930 change in near-surface air temperature (ΔT_{global}); global integrals of the local feedbacks equal the
 931 global-mean feedbacks. Top row shows net feedback (λ_{Net}) from total all-sky changes in ΔN ,
 932 second row shows $\lambda_{\text{ClearSky}}$ from changes in ΔN attributable to clear-sky radiation, third row
 933 shows cloud radiative effects (λ_{CRE}); rows 1–3 use direct model output. Fourth row shows
 934 radiative-kernel estimates of shortwave cloud feedbacks ($\lambda_{\text{Cloud}}^{\text{SW}}$). **a**, 2xCO₂ multi-model mean
 935 based on five AGCM simulations using LongRunMIP³⁴ pattern. **b**, LGM multi-model mean
 936 based on five AGCM simulations using LGMR¹⁰ pattern. **c**, LGM multi-pattern mean in CAM5
 937 using four LGM reconstructions. Note that radiative-kernel results for $\lambda_{\text{Cloud}}^{\text{SW}}$ exclude HadGEM3
 938 due to output limitations.

939
940



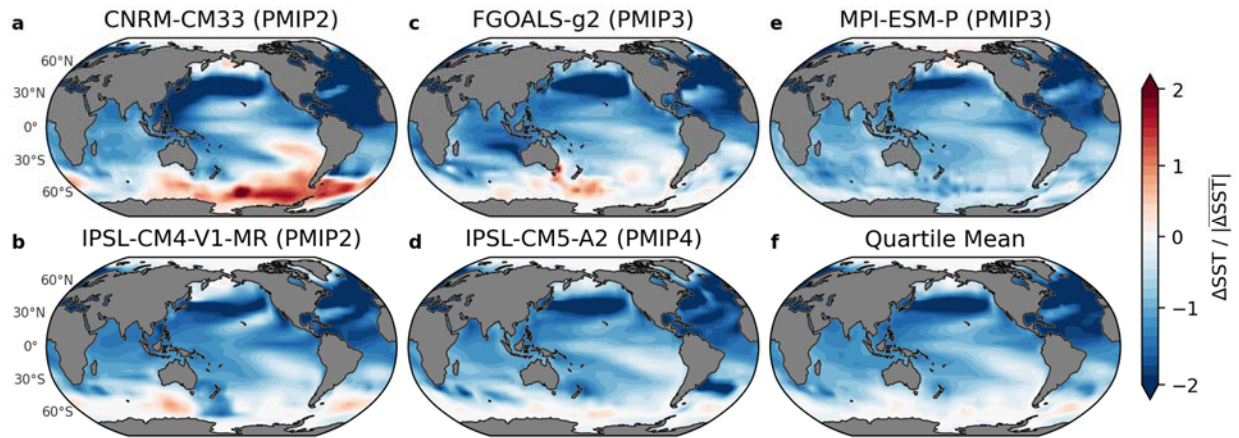
941
 942 **Extended Data Fig. 8 | Separating pattern and temperature dependence of feedback**
 943 **changes as total $\Delta\lambda \approx \Delta\lambda_{\text{PatternOnly}} + \Delta\lambda_T$.** First column shows total $\Delta\lambda = \lambda_{2x} - \lambda_{\text{LGM}}$ from Figure
 944 2, calculated in main simulations with full SST anomalies and SIC for $2x\text{CO}_2$ and LGM (using
 945 LGMR reconstruction). Second column shows pattern-only simulations with global-mean ΔSST
 946 scaled to -0.5 K , where $\Delta\lambda_{\text{PatternOnly}} \approx \lambda_{2x}^{-0.5\text{K}} - \lambda_{\text{LGM}}^{-0.5\text{K}}$. Third column shows temperature
 947 dependence, $\Delta\lambda_T$, approximated as the residual difference between the main and pattern-only
 948 simulations, $\Delta\lambda_T \approx \Delta\lambda - \Delta\lambda_{\text{PatternOnly}}$. **a**, Results in CAM4. **b**, Results in CAM5. **c**, Results in
 949 CAM6.

950
 951



952
 953
 954
 955
 956
 957
 958
 959
 960
 961
 962
 963
 964

Extended Data Fig. 9 | Likelihoods for LGM line of evidence with separate updates for SST pattern effects and temperature dependence of feedbacks. (Dotted) WCRP20 LGM likelihood¹, which includes an estimate of $\Delta\lambda_T$ for the LGM but no adjustment for pattern effects. (Dash-dot) Revised likelihood using WCRP20 estimate of $\Delta\lambda_T$ but including feedback changes from SST patterns based on pattern-only simulations in this study, assuming $\Delta\lambda_{PatternOnly} \sim \mathcal{N}(\mu = -0.51, \sigma = 0.23) \text{ Wm}^{-2}\text{K}^{-1}$. (Solid) Revised likelihood using total revised $\Delta\lambda$ from this study, as shown in Fig. 4, which includes both pattern effects and temperature dependence, assuming $\Delta\lambda \sim \mathcal{N}(-0.37, 0.23) \text{ Wm}^{-2}\text{K}^{-1}$. **a**, All likelihoods assume $\Delta T_{LGM} \sim \mathcal{N}(-5, 1)$ K as in original WCRP20 results¹. **b**, All likelihoods assume $\Delta T_{LGM} \sim \mathcal{N}(-6, 1)$ K, using the updated central estimate from IPCC AR6³.



965
 966 **Extended Data Fig. 10 | Patterns of SST anomalies from Annan¹² ensemble members in**
 967 **quartile with strongest negative climate feedback (λ).** 19 ensemble members are ranked by
 968 estimated λ (using CAM5 Green's functions²²), and 5 members shown comprise the quartile with
 969 strongest negative λ . **a-e**, Data-assimilation posterior SST using model priors specified in
 970 subtitles. **f**, Pattern of the quartile-mean SST. To show SST patterns, Local SST anomalies are
 971 normalized into patterns through division by absolute value of global-mean SST anomaly
 972 (consistent with feedbacks being calculated from radiative responses divided by global-mean
 973 temperature anomalies). All panels show annual means. LGM reconstructions are infilled to
 974 modern coastlines (Methods).

975
 976
 977
 978
 979
 980
 981
 982
 983
 984
 985
 986
 987
 988
 989
 990
 991
 992
 993

994 **Supplementary information** SI will be included as a separate document in the final version but
 995 is currently appended here for ease of review.

996
 997

998 **Supplementary information for “Last Glacial Maximum pattern**
999 **effects reduce climate sensitivity estimates”**

1000
1001 Vincent T. Cooper^{1*}, Kyle C. Armour¹, Gregory J. Hakim¹, Jessica E. Tierney², Matthew B.
1002 Osman³, Cristian Proistosescu⁴, Yue Dong⁵, Natalie J. Burls⁶, Timothy Andrews⁷, Daniel E.
1003 Amrhein⁸, Jiang Zhu⁸, Wenhao Dong⁹, Yi Ming¹⁰, and Philip Chmielewicz⁴

1004
1005 ¹ Department of Atmospheric Sciences, University of Washington, Seattle, WA, USA
1006 ² Department of Geosciences, University of Arizona, Tucson, AZ, USA
1007 ³ Department of Geography, University of Cambridge, UK
1008 ⁴ Department of Atmospheric Sciences and Department of Geology, University of Illinois at
1009 Urbana-Champaign, Urbana, IL, USA
1010 ⁵ Lamont-Doherty Earth Observatory, Columbia University, Palisades, NY, USA
1011 ⁶ Department of Atmospheric, Oceanic, and Earth Sciences, George Mason University, Fairfax,
1012 VA, USA
1013 ⁷ Met Office Hadley Centre, Exeter, UK
1014 ⁸ Climate and Global Dynamics Laboratory, National Center for Atmospheric Research, Boulder,
1015 CO, USA
1016 ⁹ NOAA/Geophysical Fluid Dynamics Laboratory, Princeton, NJ, USA
1017 ¹⁰ Earth and Environmental Sciences and Schiller Institute for Integrated Science and Society,
1018 Boston College, MA, USA
1019

1020 ***Corresponding author:** Vince Cooper (vcooper@uw.edu)
1021
1022

1023 **Contents**
1024 SI Tables 1-3: AGCM Simulation Results
1025 SI Section 1: Forcing Efficacy and Pattern Effects
1026 SI Section 2: LGM Pattern Effects in Coupled Models
1027 SI Section 3: Preparation of SST/SIC Boundary Conditions
1028 SI Section 4: Uncertainty of $\Delta\lambda$
1029 SI Section 5: Zonal-mean Feedbacks
1030

1031 **SI Tables**

1032

1033 **SI Table 1 | LGM pattern effect and climate feedbacks in various AGCMs**

1034 LGM pattern effect ($\Delta\lambda$) calculated as difference in net feedbacks (λ) from 2xCO₂ and LGM. λ_{2x}
 1035 is calculated in AGCM simulations with LongRunMIP³⁴-2xCO₂ pattern of SST/SIC. λ_{LGM} is
 1036 calculated in AGCM simulations with LGMR¹⁰ pattern. In two rightmost columns, alternative
 1037 values for ($\Delta\lambda$) are shown using 150-year regression of abrupt-4xCO₂ from coupled models
 1038 corresponding to each AGCM²¹. ζ is assumed to be 0.06 based on WCRP20's central estimate¹.
 1039

$[Wm^{-2}K^{-1}]$	$\Delta\lambda = \lambda_{2x} - \lambda_{LGM}$	λ_{2x} LongRunMIP	λ_{LGM} LGMR	$\Delta\lambda = \lambda_{4x(150yr)} / (1 + \zeta) - \lambda_{LGM}$ $\zeta = 0.06$	$\lambda_{4x(150yr)}$
CAM4	-0.45	-1.47	-1.02	-0.14	-1.23
CAM5	-0.31	-1.05	-0.74	-0.35	-1.15
CAM6	-0.63	-0.83	-0.19	-0.43	-0.66
GFDL-AM4	-0.33	-0.92	-0.60	-0.22	-0.86
HadGEM3- GC3.1-LL	-0.27	-0.62	-0.34	-0.25	-0.63
Mean	-0.40	-0.98	-0.58	-0.28	-0.91
<i>Std. Dev.</i>	<i>0.15</i>	<i>0.32</i>	<i>0.32</i>	<i>0.11</i>	<i>0.28</i>

1040

1041

1042 **SI Table 2 | LGM pattern effect and climate feedbacks from various SST patterns**
1043 LGM pattern effect ($\Delta\lambda$) from net feedbacks (λ) in 2xCO₂ and with various LGM patterns of
1044 SST/SIC. λ_{2x} is calculated in AGCMs with LongRunMIP³⁴-2xCO₂ pattern of SST/SIC. λ_{LGM} is
1045 calculated in AGCM simulations with four LGM patterns. Global-mean anomalies for SST, near-
1046 surface air temperature (T), and top-of-atmosphere radiative imbalance (N) are shown for
1047 reference. Rightmost column shows values for LGM pattern effect using 150-year regression of
1048 abrupt-4xCO₂ from coupled models²¹. ζ is assumed to be 0.06 based on WCRP20 central
1049 estimate¹.
1050
1051

	$\Delta\lambda = \lambda_{2x} - \lambda_{LGM}$ $Wm^{-2}K^{-1}$	λ $Wm^{-2}K^{-1}$	$\Delta\overline{SST}$ K	$\Delta\overline{T}$ K	$\Delta\overline{N}$ Wm^{-2}	$\Delta\lambda = \lambda_{4x(150yr)}/(1+\zeta) - \lambda_{LGM}$ $Wm^{-2}K^{-1}$
CAM4						
LGMR	-0.45	-1.02	-3.79	-5.06	5.14	-0.14
lgmDA	-0.69	-0.78	-3.14	-4.16	3.24	-0.38
Amrhein	-0.48	-0.99	-2.21	-3.38	3.36	-0.17
Annan	-0.29	-1.17	-2.18	-3.36	3.95	0.01
Mean_{CAM4}	-0.48	-0.99	-2.83	-3.99	3.92	-0.17
<i>StdDev_{CAM4}</i>	<i>0.16</i>	<i>0.16</i>	<i>0.78</i>	<i>0.80</i>	<i>0.87</i>	<i>0.16</i>
<i>2xCO₂</i>	—	-1.47	2.35	3.08	-4.52	—
CAM5						
LGMR	-0.31	-0.74	-3.79	-5.15	3.81	-0.35
lgmDA	-0.51	-0.54	-3.14	-4.24	2.27	-0.55
Amrhein	-0.33	-0.72	-2.21	-3.40	2.44	-0.37
Annan	-0.09	-0.97	-2.18	-3.38	3.28	-0.11
Mean_{CAM5}	-0.31	-0.74	-2.83	-4.05	2.95	-0.34
<i>StdDev_{CAM5}</i>	<i>0.18</i>	<i>0.18</i>	<i>0.78</i>	<i>0.84</i>	<i>0.72</i>	<i>0.18</i>
<i>2xCO₂</i>	—	-1.05	2.35	3.09	-3.24	—
Mean_{CAM4&5}	-0.39	-0.86	-2.83	-4.01	3.41	-0.26
<i>StdDev_{CAM4&5}</i>	<i>0.21</i>	<i>0.21</i>	<i>0.72</i>	<i>0.76</i>	<i>0.90</i>	<i>0.18</i>

1052
1053

1054 **SI Table 3 | Climate feedbacks and temperature dependence from pattern-only simulations**

1055 $\Delta\lambda_{\text{PatternOnly}}$ from pattern-only simulations, where LongRunMIP³⁴-2xCO₂ and LGMR¹⁰ patterns

1056 of SST anomalies are scaled to global-mean ΔSST of -0.5 K. Feedback dependence on global-

1057 mean temperature ($\Delta\lambda_{\text{T}}$) is estimated as the residual between $\Delta\lambda$ in main simulations and

1058 $\Delta\lambda_{\text{PatternOnly}}$, i.e., assuming $\Delta\lambda = \Delta\lambda_{\text{PatternOnly}} + \Delta\lambda_{\text{T}}$. Note that total $\Delta\lambda = \lambda_{2x} - \lambda_{\text{LGM}}$.

1059

$Wm^{-2}K^{-1}$	$\lambda_{2x}^{-0.5K}$	$\lambda_{\text{LGM}}^{-0.5K}$	$\Delta\lambda_{\text{Only}}^{\text{Pattern}} = \lambda_{2x}^{-0.5K} - \lambda_{\text{LGM}}^{-0.5K}$	$\Delta\lambda_{\text{T}} = \Delta\lambda - \Delta\lambda_{\text{Only}}^{\text{Pattern}}$	$\Delta\lambda = \Delta\lambda_{\text{Only}}^{\text{Pattern}} + \Delta\lambda_{\text{T}}$, $\Delta\lambda = \lambda_{2x} - \lambda_{\text{LGM}}$
CAM4	-1.98	-1.55	-0.42	-0.03	-0.45
CAM5	-1.59	-1.24	-0.35	0.04	-0.31
CAM6	-1.30	-0.55	-0.75	0.12	-0.63
Mean	-1.63	-1.12	-0.51	0.04	-0.47

1060

1061

1062

1063 **SI Section 1: Forcing Efficacy and Pattern Effects**

1064 In this section, we briefly consider the relationship between “efficacy” and pattern
1065 effects, which is explored in detail in Zhou et al. (2023)⁴⁸. The efficacy framework translates one
1066 unit of forcing by a non-CO₂ agent, e.g., ice sheets, into the equivalent amount of CO₂ forcing
1067 which would cause the same global-mean ΔT . While past research on forcing efficacy has
1068 considered that different forcings have different temperature impacts⁸⁶, analyses using the
1069 efficacy framework for the LGM have produced disparate results^{25,26,40,41,43,87}, possibly due to
1070 simplified physics of intermediate-complexity models^{40,41}. Because of these results, WCRP20
1071 inflates uncertainty on LGM forcings.

1072 Efficacy, ϵ , can be equivalently framed as a ratio of radiative feedbacks, e.g., $\epsilon_{\text{IceSheet}} =$
1073 $\lambda_{2x} / \lambda_{\text{IceSheet}}$. The negative LGM pattern effect ($\Delta\lambda = \lambda_{2x} - \lambda_{\text{LGM}}$, $\Delta\lambda < 0$), which we find in
1074 AGCM simulations using data-assimilation reconstructions for the LGM, is consistent with an
1075 LGM efficacy > 1 . The efficacy of ice sheets is greater than 1 in the following model-only
1076 studies with mixed-layer oceans coupled to atmospheric general circulation models: CESM1-
1077 CAM5²⁶, CESM2⁴³, and CESM2-PaleoCalibr⁴⁴ (SI Section 2). Some intermediate-complexity
1078 models^{40,41}, however, have reported ice-sheet efficacy < 1 .

1079 The pattern effect, combined with temperature dependence, can equivalently explain
1080 forcing efficacy⁴⁸. We use the pattern-effect framework rather than efficacy because it allows for
1081 quantification of feedback changes in AGCMs using observational constraints on SST patterns
1082 from data assimilation and has strong theoretical underpinnings^{5,22,48}. The pattern-effect
1083 framework is oriented around the climate feedback, λ , which is the key uncertain parameter for
1084 climate sensitivity. We follow methods in WCRP20¹ to account for $\Delta\lambda$ for the LGM in estimates
1085 of modern-day climate sensitivity. We refer readers to Zhou et al. (2023)⁴⁸ for further
1086 explanation of the connection between efficacy and pattern-effect frameworks.

1087

1088 *Additional references:*

1089 86. Hansen, J. *et al.* Efficacy of climate forcings. *Journal of Geophysical Research: Atmospheres* **110**, 1–
1090 45 (2005).

1091 87. Yoshimori, M., Yokohata, T. & Abe-Ouchi, A. A Comparison of Climate Feedback Strength between
1092 CO₂ Doubling and LGM Experiments. *J Clim* **22**, 3374–3395 (2009).

1093

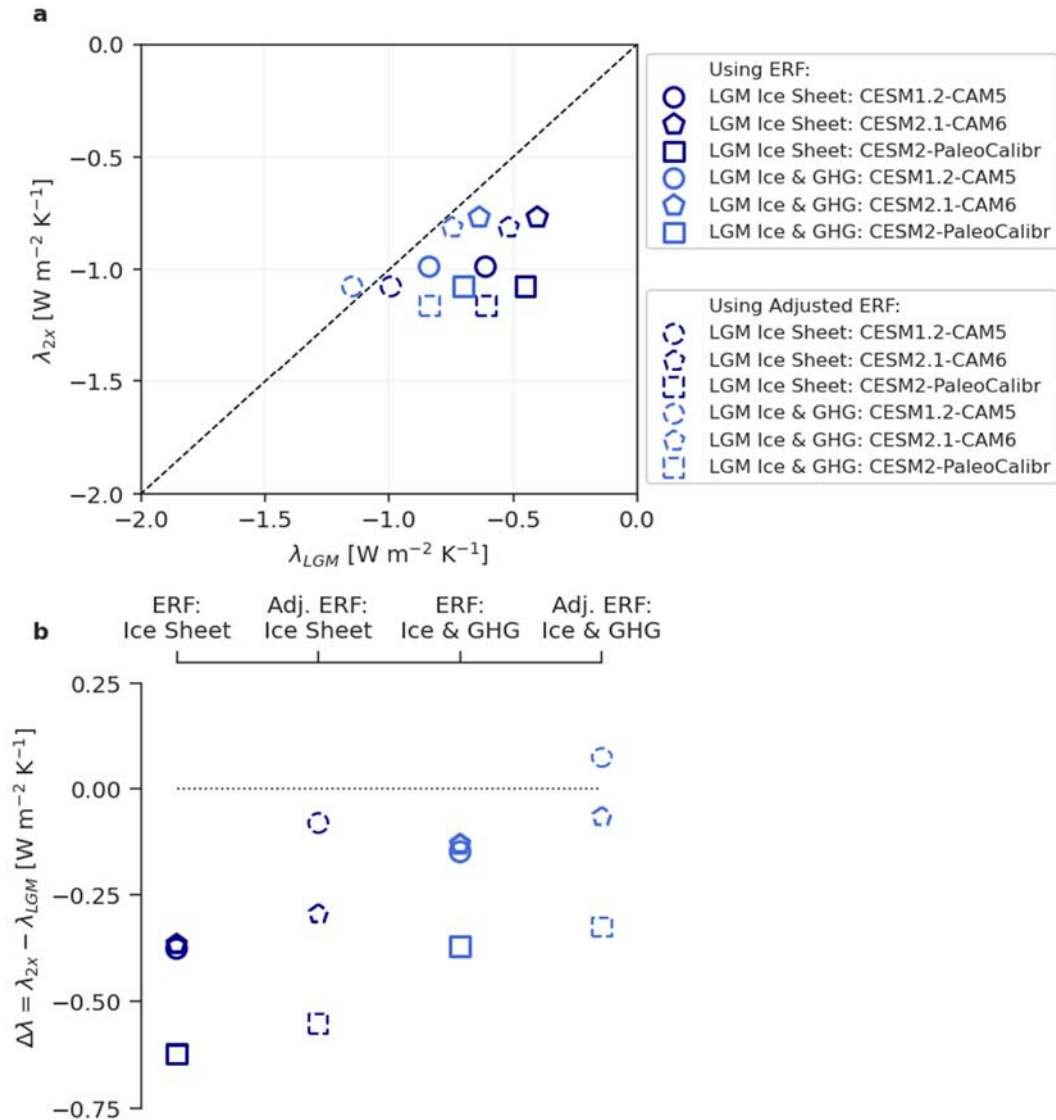
1094

1095

1096 **SI Section 2: LGM Pattern Effects in Coupled Models**

1097 Simulations with mixed-layer ocean models coupled to AGCMs (known as slab ocean
1098 models⁴⁵, “SOM” hereafter) in CESM1-CAM5²⁶, CESM2.1-CAM6⁴³, and CESM2-PaleoCalibr⁴⁴
1099 illustrate pattern effects in coupled models. Note that feedbacks from ocean dynamics are
1100 excluded in the SOM, and models’ SST/SIC patterns are not constrained by proxy data, hence
1101 we use the SOM only to support interpretation of the LGM pattern effect. Feedbacks in SOM
1102 simulations are calculated as $\lambda = \Delta \text{ERF} / \Delta T$, where the effective radiative forcing (ERF) is
1103 determined from introducing forcings in separate simulations in the corresponding AGCMs
1104 (keeping SST/SIC fixed at pre-industrial values), and ΔT is the equilibrium change in global-
1105 mean near-surface air temperature in the SOM (also known as reference-height temperature, or
1106 “TREFHT” in CESM name conventions). The ERF is affected by changes in land-surface
1107 temperatures, which are not held constant in AGCM simulations due to practical limitations, and
1108 an adjustment^{26,86} to the ERF can be made to account for land changes—see Zhu & Poulsen
1109 (2021)²⁶ for methods.

1110 This adjustment (based on the climate sensitivity parameter²⁶) can also be applied to
1111 estimate an “adjusted ERF” for LGM ice sheets, although it is difficult to assess the validity of
1112 the adjustment for ice-sheet forcing, which affects not only land temperatures but also
1113 topography. Radiative kernels based on modern climate would typically be used to validate the
1114 ERF adjustment²⁶, but they cannot be applied with LGM topography. Figure S2.1 shows
1115 feedbacks using both ERF and adjusted ERF. Note that these values do not affect our
1116 quantification of $\Delta \lambda$ in ECS calculations.



1117
 1118
 1119
 1120
 1121
 1122
 1123
 1124
 1125
 1126
 1127
 1128
 1129
 1130

Figure S2.1 | Feedbacks and $\Delta\lambda$ using either effective radiative forcing (ERF) or adjusted ERF from previously published simulations in mixed-layer ocean models. a, Scatter plot of λ_{2x} vs. λ_{LGM} in mixed-layer ocean models; λ_{LGM} is shown for simulations using only the LGM ice-sheet forcing (dark blue), which includes LGM sea-level changes, and for simulations using LGM ice-sheet forcing and greenhouse-gas (GHG) forcings (royal blue). Dashed markers indicate corresponding results using “adjusted ERF” to calculate feedbacks. **b**, $\Delta\lambda$ based on feedbacks shown in panel **a**. Note that in LGM simulations using CESM2.1-CAM6⁴³ and CESM2-PaleoCalibr⁴⁴, the LGM ice-sheet forcing and GHG forcing are applied in separate simulations, and their sums are shown as LGM Ice & GHG. This linearity assumption was validated in CESM1-CAM5²⁶.

1131 **SI Section 3: Preparation of SST/SIC Boundary Conditions**

1132 SST and SIC boundary conditions (BCs) for the LGM, Late Holocene baseline, and
1133 2xCO₂ are prepared to enable consistent calculation of the net feedback (λ) that is applicable to a
1134 modern-day doubling of CO₂. When changing the surface BCs in AGCM simulations to compute
1135 λ , $\Delta F=0$ in equation (1) only if there are no changes in land-sea distribution or ice-sheets. For the
1136 LGM and Late Holocene datasets, we adjust for differences in land-sea distribution compared to
1137 present day using kriging and extrapolation near coastlines in polar regions.

1138 For SST, kriging is performed across overlapping subset regions of radius ≈ 3000 km
1139 spaced around the globe. Results for overlapping subset regions are merged using inverse-
1140 distance weighting from the center of each subset region. Kriging results are retained only where
1141 no pre-existing SST value exists in a dataset. Over polar regions and inland waters, inverse-
1142 distance extrapolation populates the SST field.

1143 For SIC, all values are first required to be no less than the ice-sheet fraction at that
1144 location, i.e., modern seas that were covered by ice sheets at the LGM, such as the Hudson Bay,
1145 are assigned a minimum SIC that equals the LGM ice fraction at 21,000 years ago⁵⁴. For modern
1146 seas which were land but not ice sheet at the LGM, SIC is populated based on the SST. This step
1147 uses the SIC formula from the CAM boundary condition protocol⁸⁸, where SIC=100% if SST < -
1148 1.8°C, SIC = 0% if SST > 4.97°C, and otherwise the infilled SIC = $0.729 - ((\text{SST} +$
1149 $1.8)/9.328)^{1/3}$. Gaussian smoothing is applied to the result, reducing any sharp boundaries caused
1150 by the infilling. The SIC formula above is also applied to maintain internally consistent values of
1151 SST and SIC⁸⁸ in the Late Holocene baseline. See SI Section 4 for uncertainty tests regarding sea
1152 ice.

1153 The Annan dataset includes only annual SST and no reconstruction of SIC. Because SIC
1154 is required in all AGCMs, we assign the SIC from Amrhein to the Annan data. In a CAM4 test
1155 using the LGMR SIC with Annan SSTs (instead of the Amrhein SIC), $\Delta\lambda$ is marginally more
1156 negative (λ_{LGM} changes by $< 0.1 \text{ Wm}^{-2}\text{K}^{-1}$). This result suggests that uncertainty from assigning
1157 a SIC reconstruction to Annan SSTs is small compared to uncertainty in the SST reconstruction.
1158 We assign the Amrhein SIC for the Annan SST in our main results because this choice is more
1159 conservative in that it reduces the magnitude of the mean LGM pattern effect. For consistency,
1160 the Annan SST is assigned the annual cycle from the Amrhein data for SST/SIC.

1161 For the 2xCO₂ BC, we use output from LongRunMIP simulations of abrupt and transient-
1162 1% yr⁻¹ doubling of CO₂. We use the mean of 200 years of output from the following six models
1163 to create a multi-model mean SST/SIC BC: CESM1.0.4 (years 2300-2500), CNRM-CM6-1
1164 (years 550-750), HadCM3L (years 500-700), MPI-ESM-1.2 (years 800-1000), GFDL-ESM2M
1165 (years 4300-4500), and MIROC3.2 (years 1803-2003). HadCM3L results use years 500-700 due
1166 to an output error in the pre-industrial control run after year 700. All LongRunMIP results are
1167 regridded to a standard 1.9° x 2.5° lat-lon grid. For SIC, monthly output is available, and we
1168 compute a 200-yr climatology for each model and then a multi-model-mean climatology. For
1169 SST, annual output is available for each model and monthly output from MIROC3.2. We
1170 compute the 200-yr mean SST anomaly for each model and then apply the annual cycle from
1171 MIROC3.2 to the multi-model mean. We also show results in Ext. Data Fig. 3-4 which do not
1172 use the LongRunMIP-2xCO₂ BC and instead use 150-yr regressions⁷⁰ of abrupt-4xCO₂ from
1173 parent coupled models corresponding to each AGCM used in this study, thereby sampling
1174 uncertainty in warming patterns because the 150-year regressions are produced from different
1175 models' warming patterns.

1176 BCs are regridded to the 1.9° x 2.5° (latitude x longitude) grid used for CAM4, CAM5,
1177 and CAM6. HadGEM3-GC31-LL regrids to N96 (resolution of approximately 135 km)⁶⁷, and
1178 GFDL-AM4 regrids to a C96 cubed sphere (resolution of approximately 100 km)⁶⁸.

1179 For the “pattern-only” simulations with SST anomalies normalized to -0.5 K, we make
1180 the following changes to the LGM and 2xCO₂ BCs. For the LGM, we use the LGMR SST. For
1181 2xCO₂, we use the LongRunMIP SST. We compute the global-mean $\overline{\Delta\text{SST}}$ for both datasets as
1182 $\overline{\Delta\text{SST}}$, and we multiply all local SST anomalies by the scale factor $-0.5/\overline{\Delta\text{SST}}$. This scaling
1183 causes the resulting global-mean ΔSST to become -0.5 K, but the spatial pattern of the SST
1184 anomalies is unchanged. We use -0.5 K for both the LGM and 2xCO₂ so that there is no
1185 cooling-warming asymmetry, and ΔT is small enough that temperature dependence of λ is
1186 negligible (i.e., $\Delta\lambda_T \approx 0$, and $\Delta\lambda \approx \Delta\lambda_{\text{PatternOnly}}$). ΔT is still large enough that we can compute
1187 $\lambda = \Delta N / \Delta T$ without requiring an excessively long simulation to overcome noise in the
1188 denominator. We use the baseline SIC (Late Holocene) in all of the pattern-only simulations so
1189 there are no changes in sea ice, so this set of simulations also serves to check whether $\Delta\lambda$ is
1190 attributable to SIC rather than SST changes.

1191 An additional simulation was run in HadGEM3-GC3.1-LL with SIC held constant at the
1192 Late Holocene baseline while the SST field is varied with the full value of anomalies, using the
1193 LongRunMIP-2xCO₂ and LGMR patterns of SST. Results from this simulation are shared in SI
1194 section 4.

1195 This concludes the preparation steps for the main simulations (BCs from four data-
1196 assimilation reconstructions for the LGM, one Late Holocene, and one 2xCO₂) and the “pattern-
1197 only” simulations (two additional BCs: LGMR_{-0.5K} and LongRunMIP-2xCO₂_{-0.5K}). The final
1198 adjustment to each BC follows the standard boundary-condition protocol for CAM, known as
1199 “bcgen.” This process ensures that SIC and SST are plausibly bounded (e.g., SIC between 0 and
1200 1), and it transfers the monthly climatology to mid-month values which can be linearly
1201 interpolated in an AGCM.

1202

1203 *Additional references:*

1204 88. Hurrell, J. W., Hack, J. J., Shea, D., Caron, J. M. & Rosinski, J. A New Sea Surface Temperature and
1205 Sea Ice Boundary Dataset for the Community Atmosphere Model. *J Clim* **21**, 5145–5153 (2008).

1206

1207

1208 **SI Section 4: Uncertainty of $\Delta\lambda$**

1209 To include the LGM pattern effect in the Bayesian framework of WCRP20, we must
1210 assign a statistical distribution to $\Delta\lambda$ for the LGM (following WCRP20’s method for $\Delta\lambda$ in the
1211 historical record). In this section we provide additional detail on combining uncertainty from
1212 AGCM physics and LGM reconstructions with bootstrapping.

1213 To evaluate the sensitivity of our uncertainty quantification to the size of our sample, we
1214 calculate a bootstrap confidence interval (CI) on our estimate, $\hat{\sigma}$, of the standard deviation of $\Delta\lambda$
1215 as follows. First, we construct a sample where each AGCM is equally weighted and the spread
1216 from various LGM reconstructions is included in the sample (as described below). We then use
1217 bootstrapping of this sample to provide confidence bounds on our estimate ($\hat{\sigma}$) of the population
1218 standard deviation from the sample standard deviation.

1219 To create the equally weighted sample, we assume that the spreads around the LGMR
1220 feedback (of the feedbacks from Amrhein, Annan, and lgmDA) would be the same in GFDL-
1221 AM4, HadGEM3-GC3.1-LL, and CAM6 as they are in CAM4 or CAM5. We include the
1222 simulations using the extreme quartiles from Annan and LGMR in the sample. This assumption

1223 yields a sample of 40 values of $\Delta\lambda$ based on (4 LGM patterns + 2 extreme-quartile LGMR
1224 patterns + 2 extreme-quartile Annan patterns) x (5 AGCMs). We proceed with bootstrapping by
1225 sampling with replacement from the 40 values of $\Delta\lambda$. We generate 10^5 samples of size $n = 19$,
1226 choosing a sample size in the bootstrap of 19 because there are only 19 actual estimates of $\Delta\lambda$
1227 from simulations in the AGCMs. This process yields 10^5 bootstrapped values of $\hat{\sigma}$ from which
1228 we derive the 95% CI: (0.15, 0.31) $\text{Wm}^{-2}\text{K}^{-1}$. Note that the upper bound of 0.31 $\text{Wm}^{-2}\text{K}^{-1}$ is
1229 much less than two times the population standard deviation of 0.23 $\text{Wm}^{-2}\text{K}^{-1}$ that we assign to
1230 $\Delta\lambda$, indicating that doubling the assumed standard deviation for $\Delta\lambda$ is a more conservative
1231 uncertainty test (Extended Data Fig. 4) than using the bootstrapped 95% bound.

1232 Sea ice reconstructions, which are not well constrained, contribute to uncertainty in the
1233 LGM pattern effect. However, the uncertainty due to sea ice appears small compared to the
1234 uncertainty across AGCM physics and in the SST pattern. In an additional set of simulations
1235 with HadGEM3-GC3.1-LL (not discussed in the main text), the SST anomalies are applied in
1236 full at the LGMR, Late Holocene, and LongRunMIP-2xCO₂ values while the SIC is held
1237 constant at the Late Holocene values. These simulations make λ_{2x} and λ_{LGM} more negative by
1238 eliminating the positive ice-albedo feedback, but the difference in the feedbacks, $\Delta\lambda$, is largely
1239 unaffected. Constant SIC produces $\Delta\lambda = -0.28 \text{ Wm}^{-2}\text{K}^{-1}$, compared to $-0.27 \text{ Wm}^{-2}\text{K}^{-1}$ in the
1240 main simulations for HadGEM3-GC3.1-LL. SIC is also held constant in the pattern-only
1241 simulations, which produce $\Delta\lambda < 0$. While our results appear robust despite uncertainty in SIC, we
1242 cannot eliminate the possibility that substantially different SIC reconstructions or SIC responses
1243 to 2xCO₂ could change the resulting $\Delta\lambda$. Future work should further examine the role of sea ice
1244 in paleoclimate pattern effects.

1245

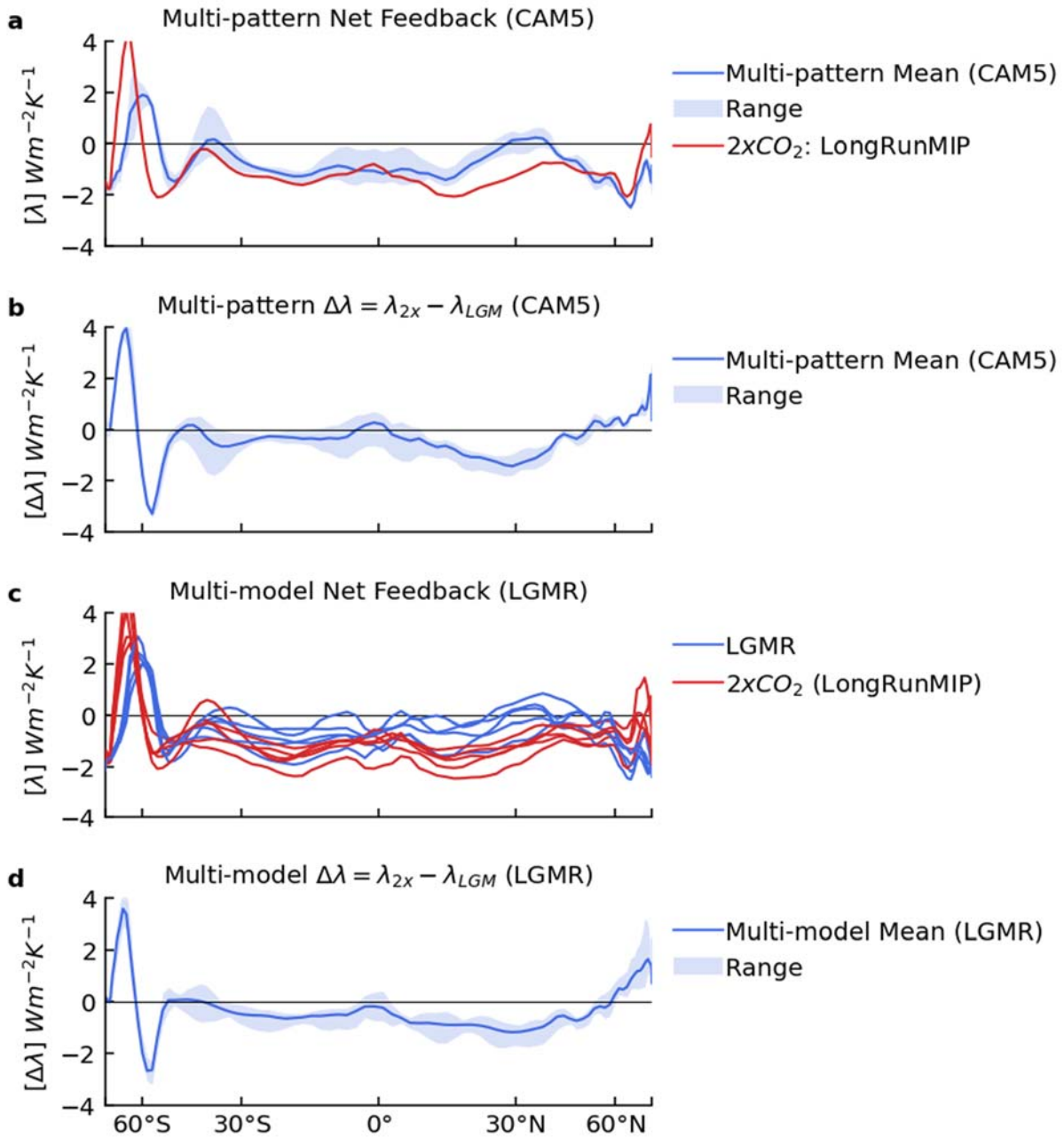
1246

1247 **SI Section 5: Zonal-mean Feedbacks**

1248 The following figures show zonal means (indicated by brackets as $[\lambda]$) of feedbacks in Extended
1249 Data Figure 6. The net feedback, clear-sky shortwave (SW), clear-sky longwave (LW), and
1250 cloud radiative effect are calculated directly from model output. The remaining feedbacks are
1251 from radiative kernel decomposition (Methods). Total cloud feedback is also shown as the sum
1252 of SW and LW components.

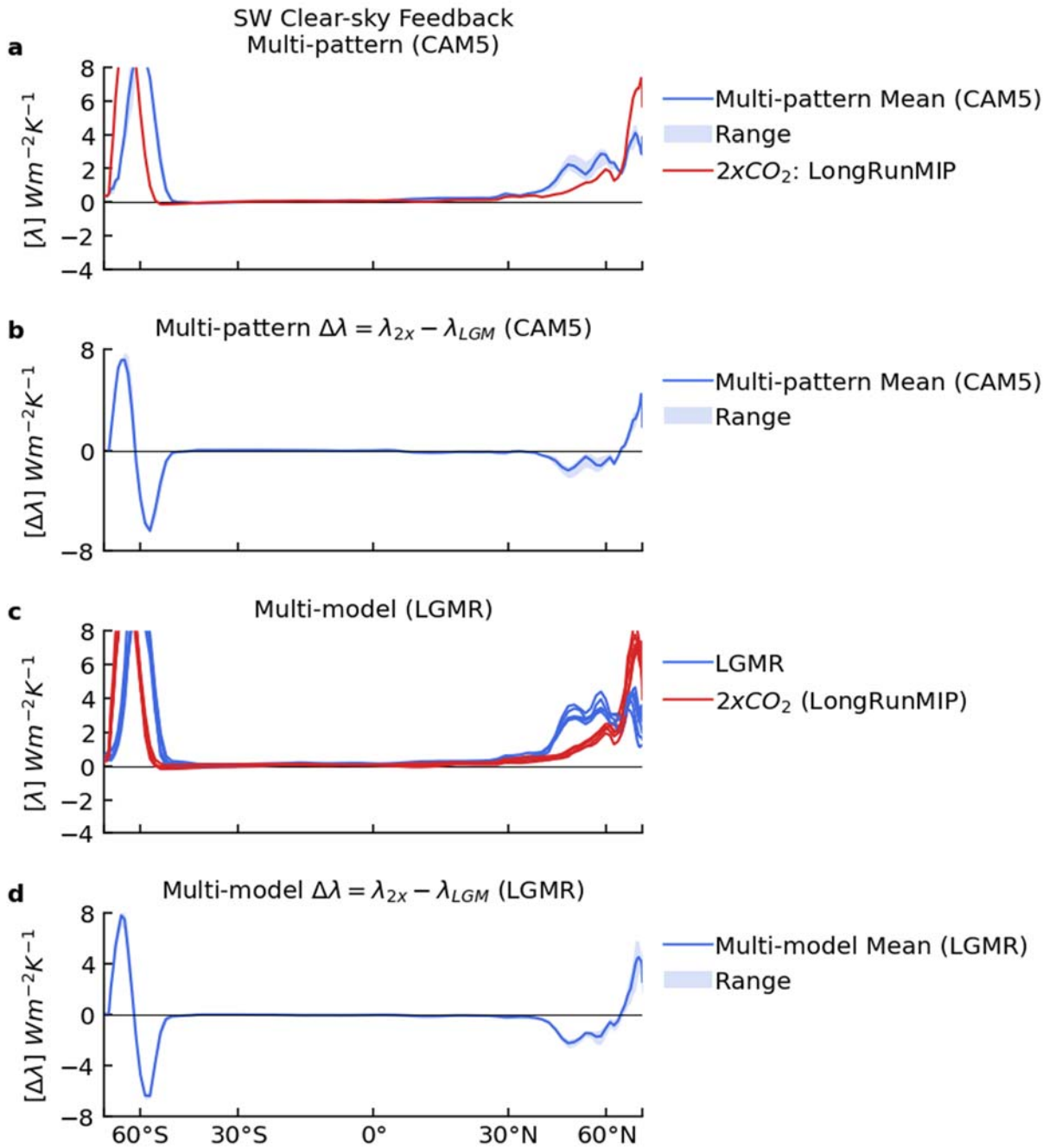
1253 Each of the following figures consists of: **a**, In CAM5, mean and range of feedbacks
1254 across four LGM reconstructions and 2xCO₂ from LongRunMIP. **b**, In CAM5, mean and range
1255 of the difference in feedbacks ($\Delta\lambda = \lambda_{2x} - \lambda_{LGM}$) across four LGM reconstructions from results in
1256 panel **a**. **c**, Feedbacks across various AGCMs, using the LGMR reconstruction of the LGM and
1257 2xCO₂ from LongRunMIP. **d**, Mean and range of $\Delta\lambda$ across various AGCMs from results in
1258 panel **c**. Note that HadGEM3 is not included in the kernel-derived feedbacks due to limited
1259 availability of model output.

1260



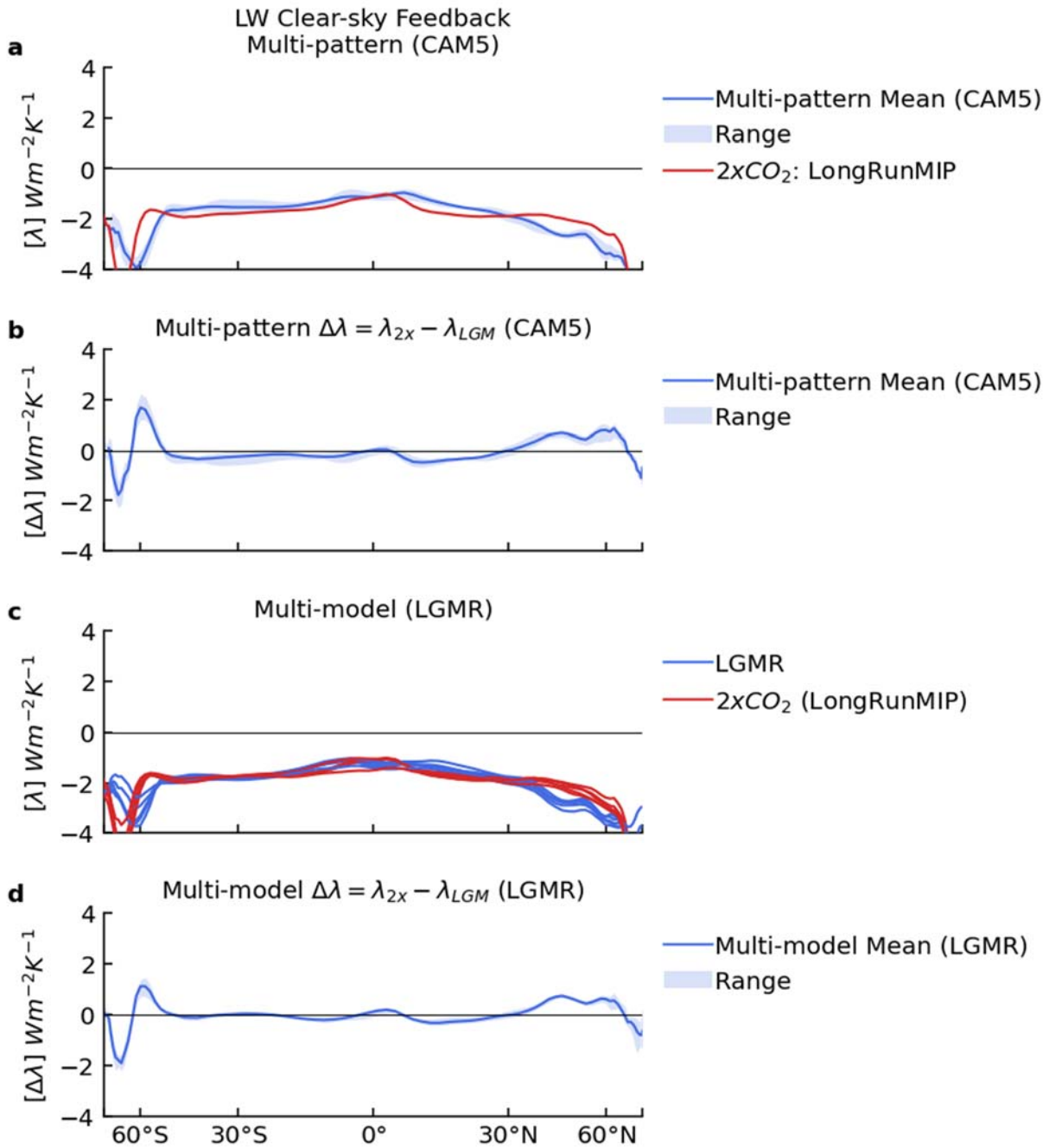
1261
 1262
 1263
 1264

SI Figure 5.1 | Net Feedback
Figure description at beginning of SI Section 5.



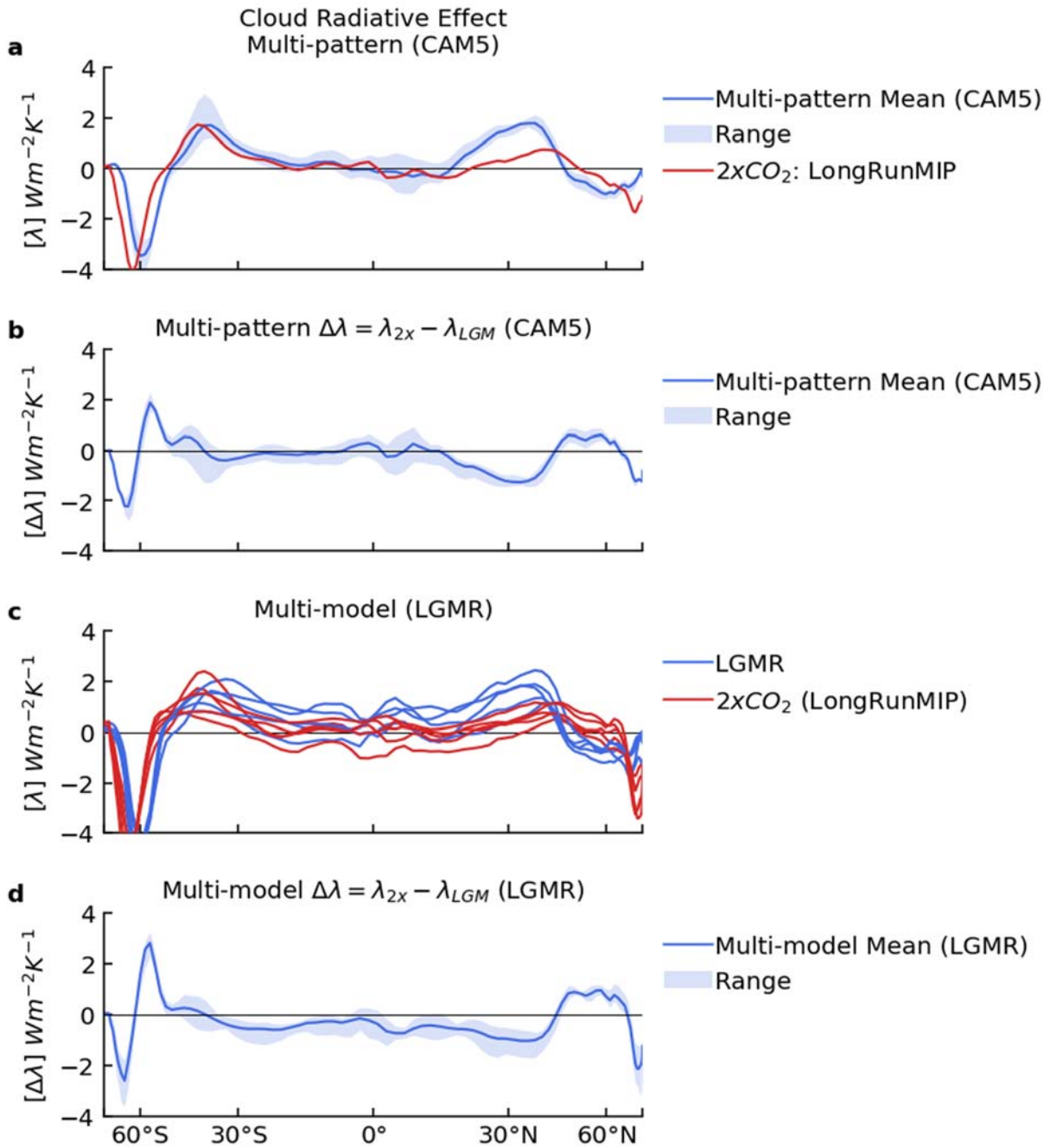
1265
1266
1267
1268
1269

SI Figure 5.2 | Clear-sky (SW) Feedback
Figure description at beginning of SI Section 5.



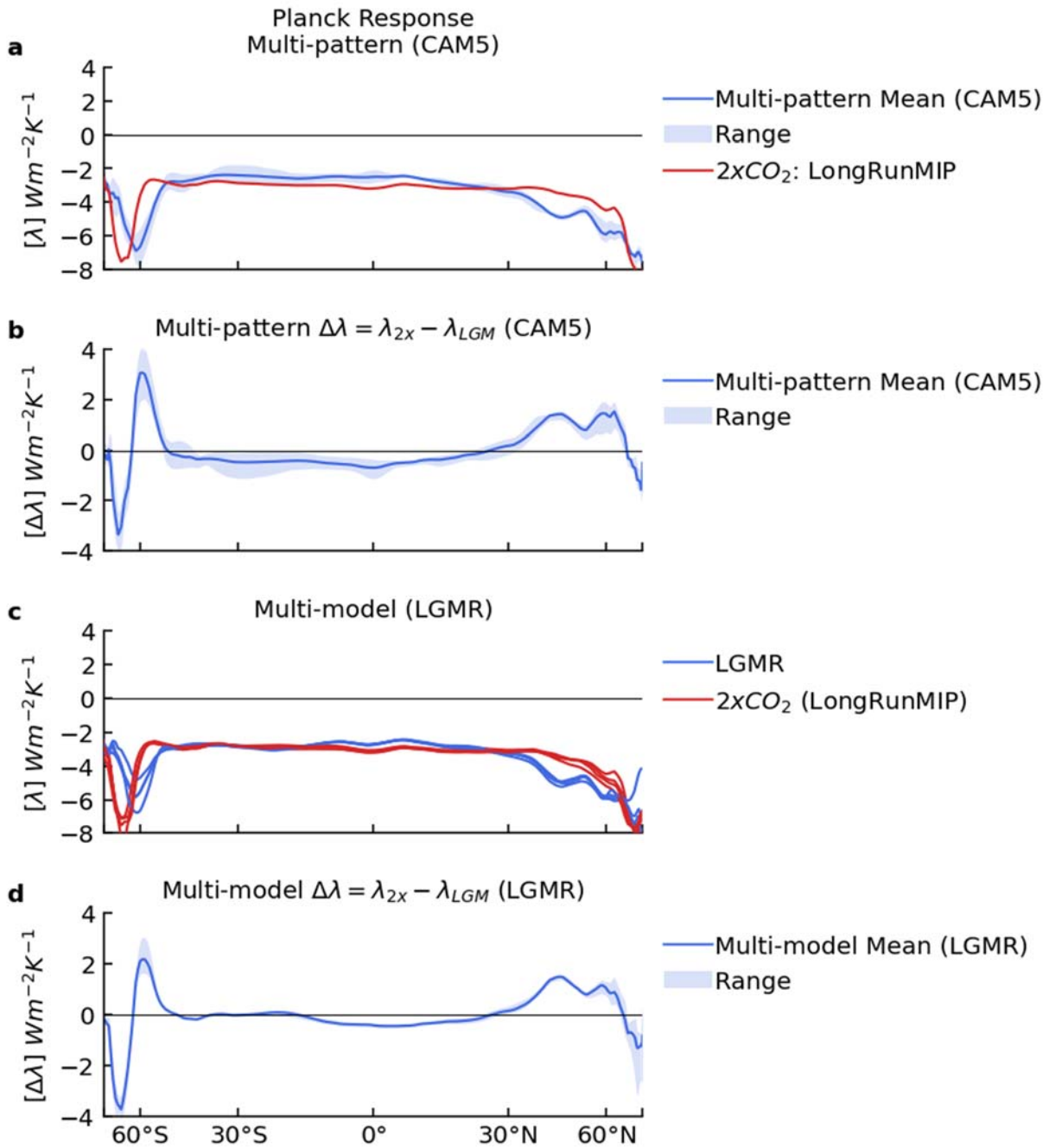
1270
1271
1272
1273
1274

SI Figure 5.3 | Clear-sky (LW) Feedback
Figure description at beginning of SI Section 5.



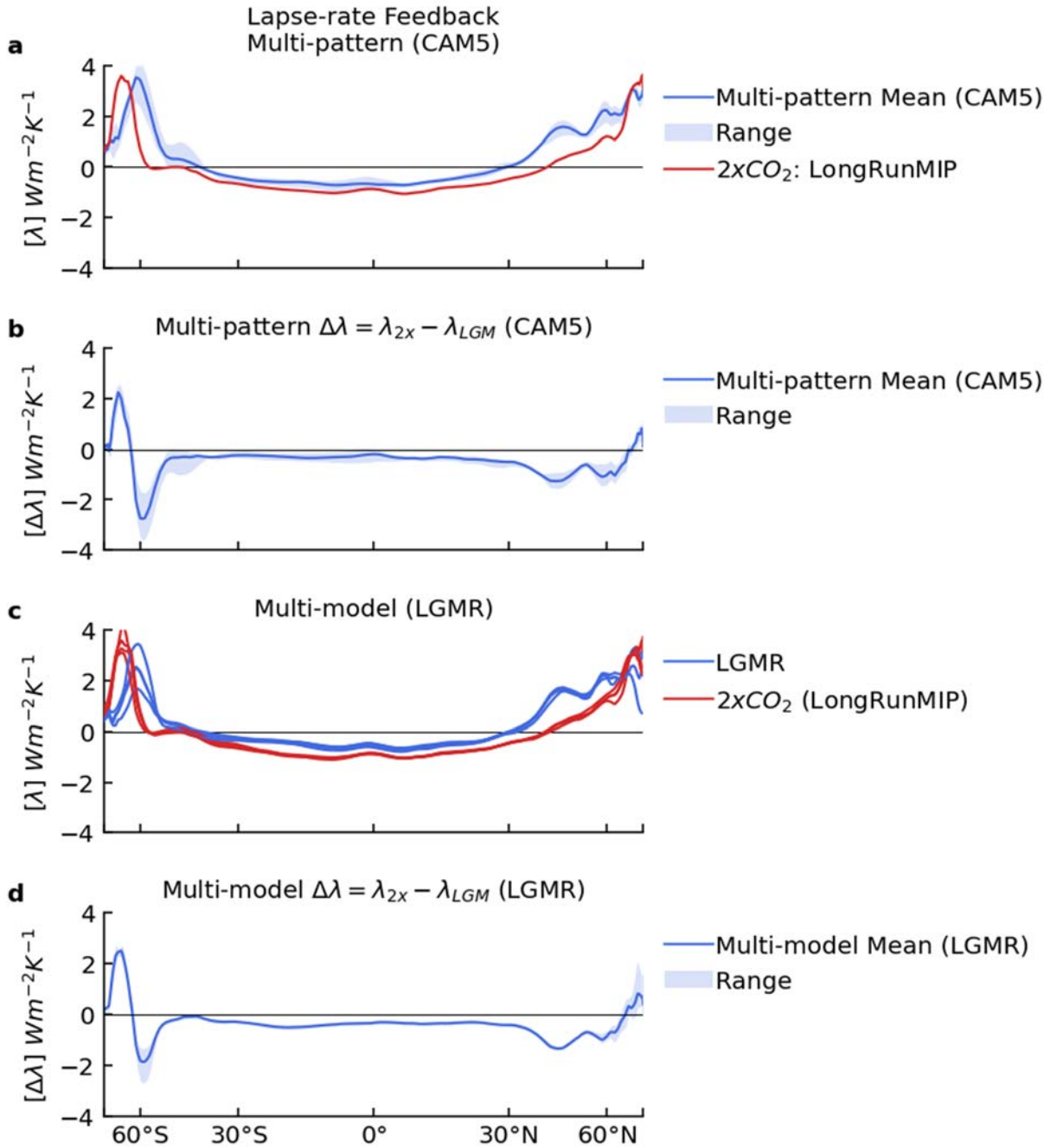
1275
1276
1277
1278
1279

SI Figure 5.4 | Cloud Radiative Effect
Figure description at beginning of SI Section 5.



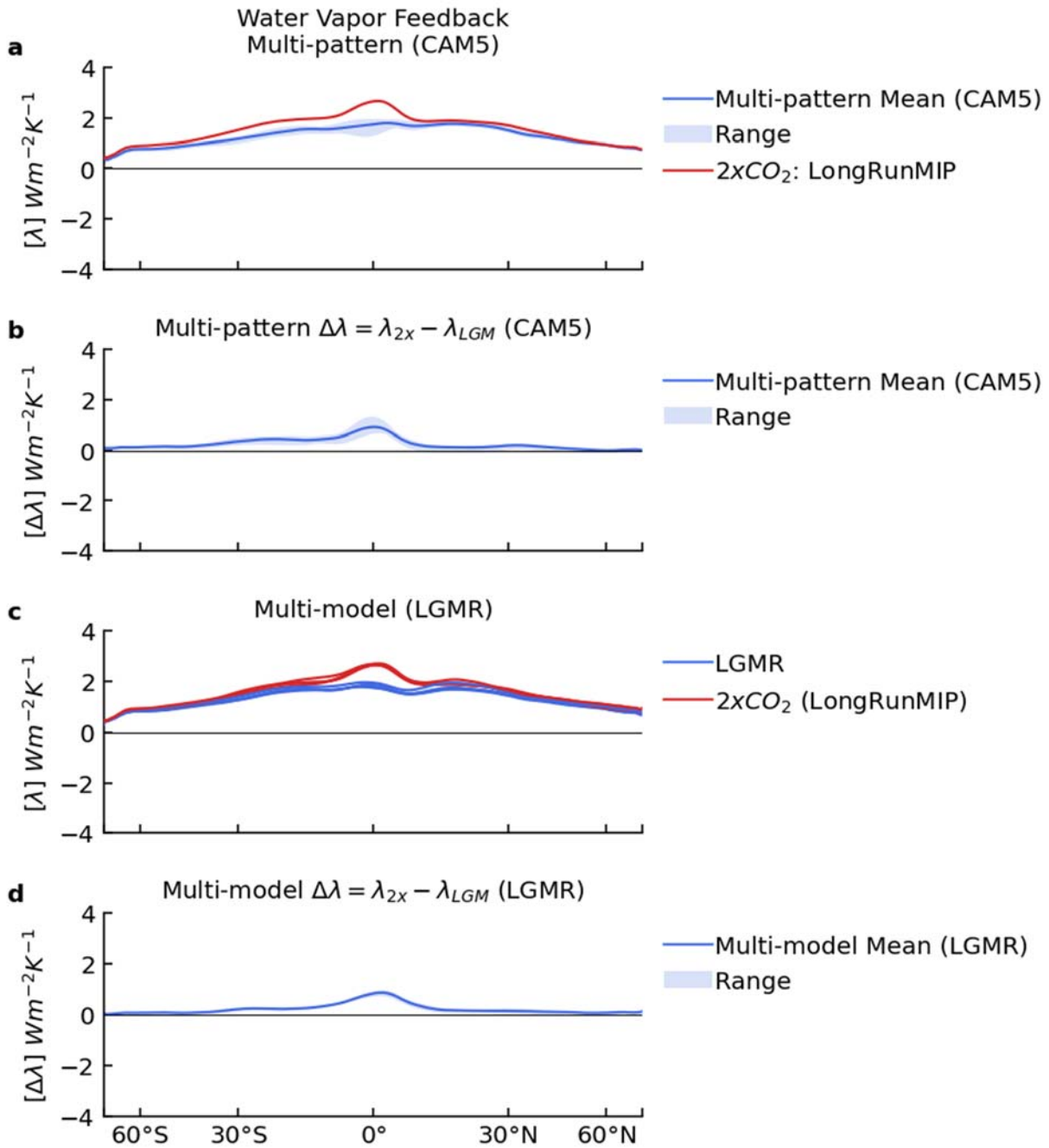
1280
 1281
 1282
 1283
 1284

SI Figure 5.5 | Planck Response
Figure description at beginning of SI Section 5.



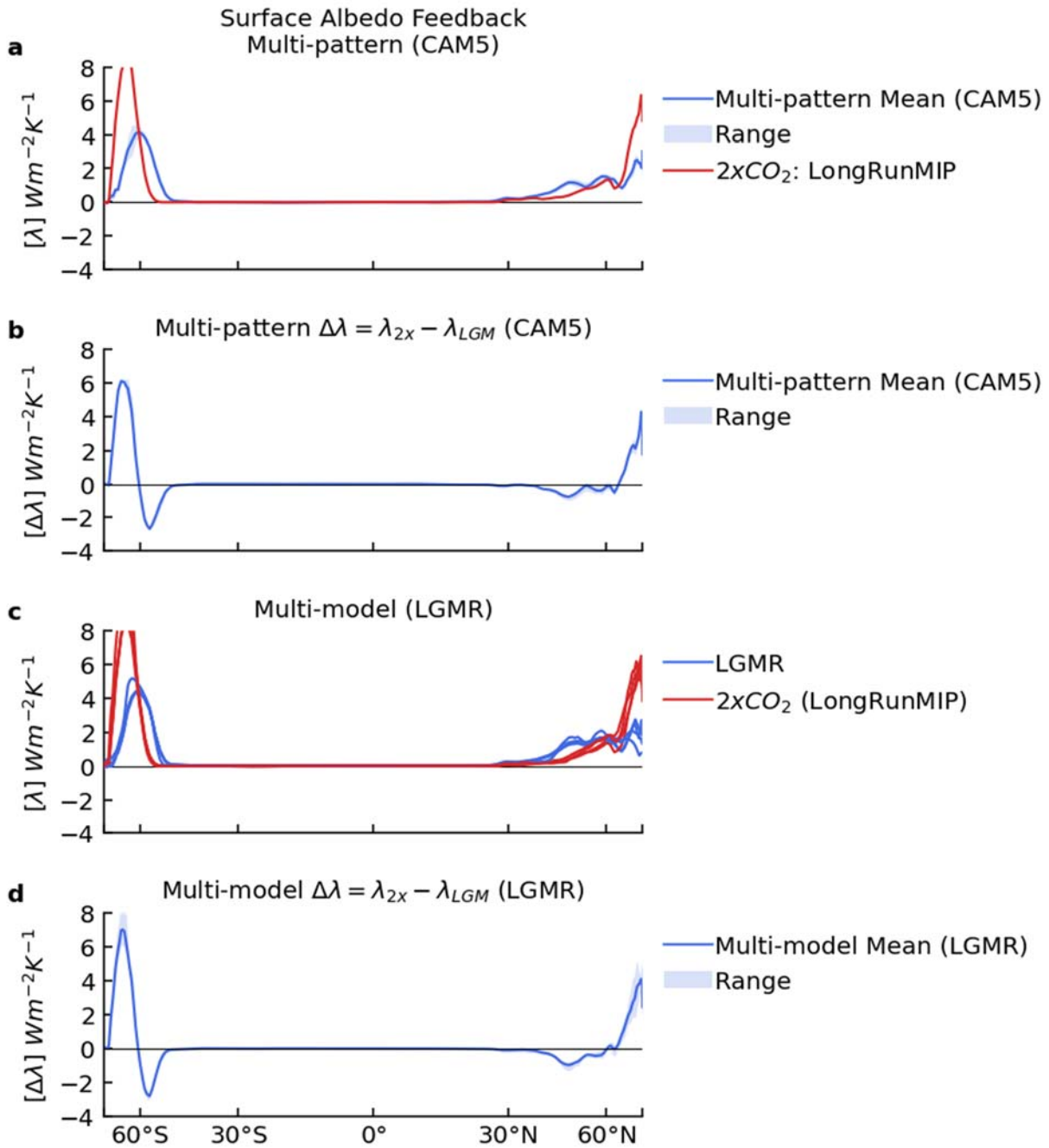
1285
 1286
 1287
 1288
 1289

SI Figure 5.6 | Lapse-rate Feedback
Figure description at beginning of SI Section 5.



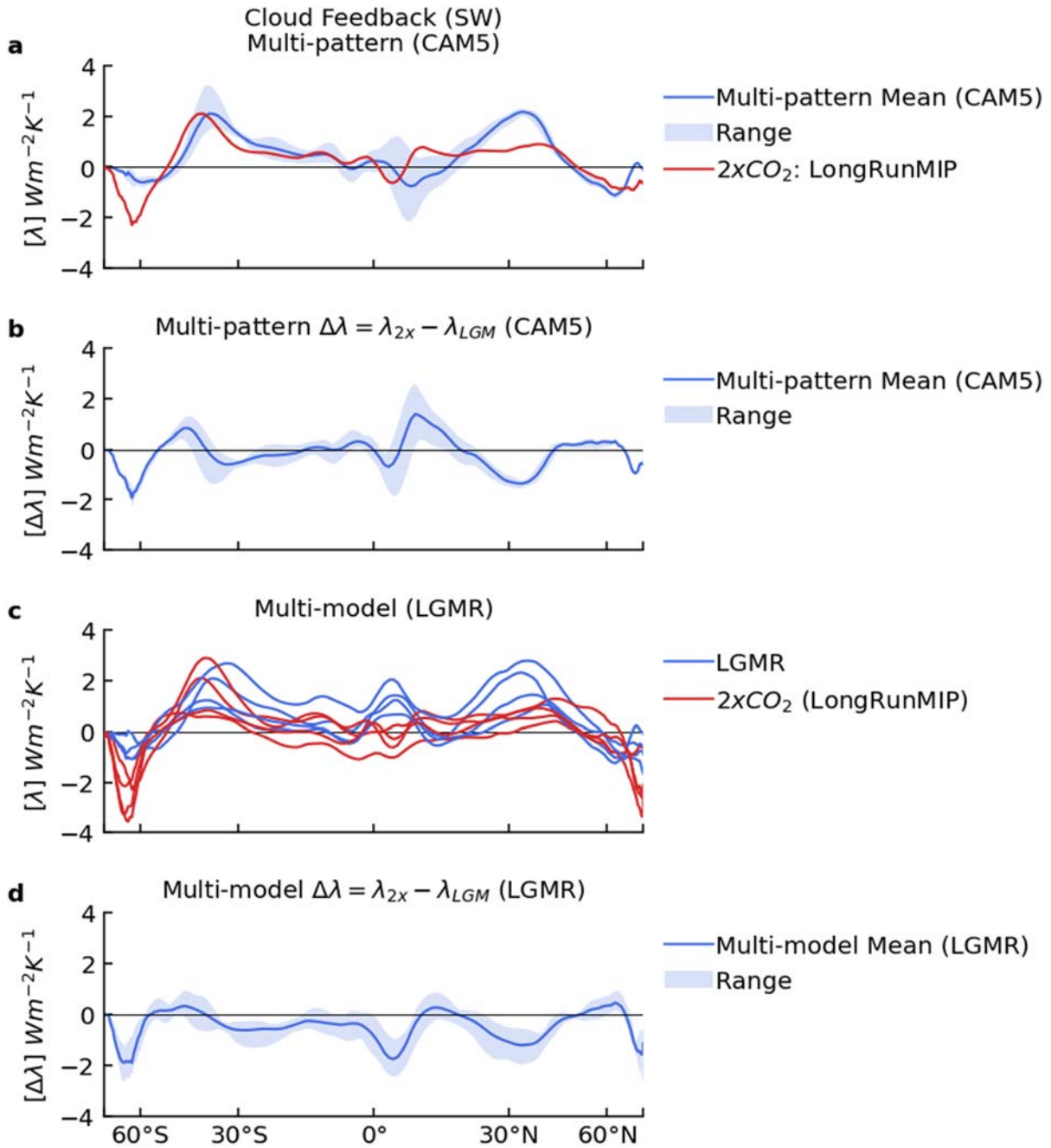
1290
1291
1292
1293
1294

SI Figure 5.7 | Water Vapor Feedback
Figure description at beginning of SI Section 5.



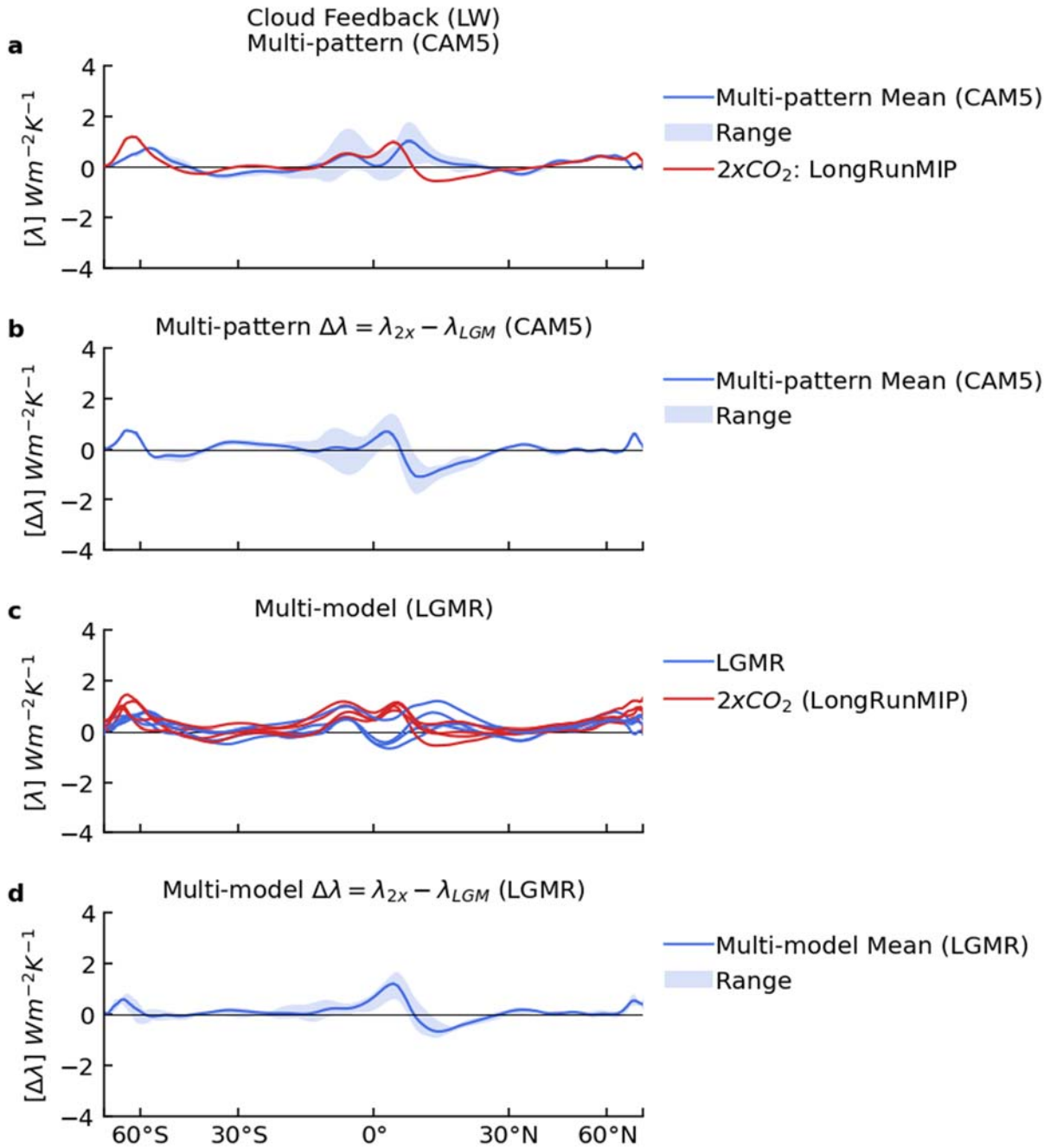
1295
1296
1297
1298
1299

SI Figure 5.8 | Surface Albedo Feedback
Figure description at beginning of SI Section 5.



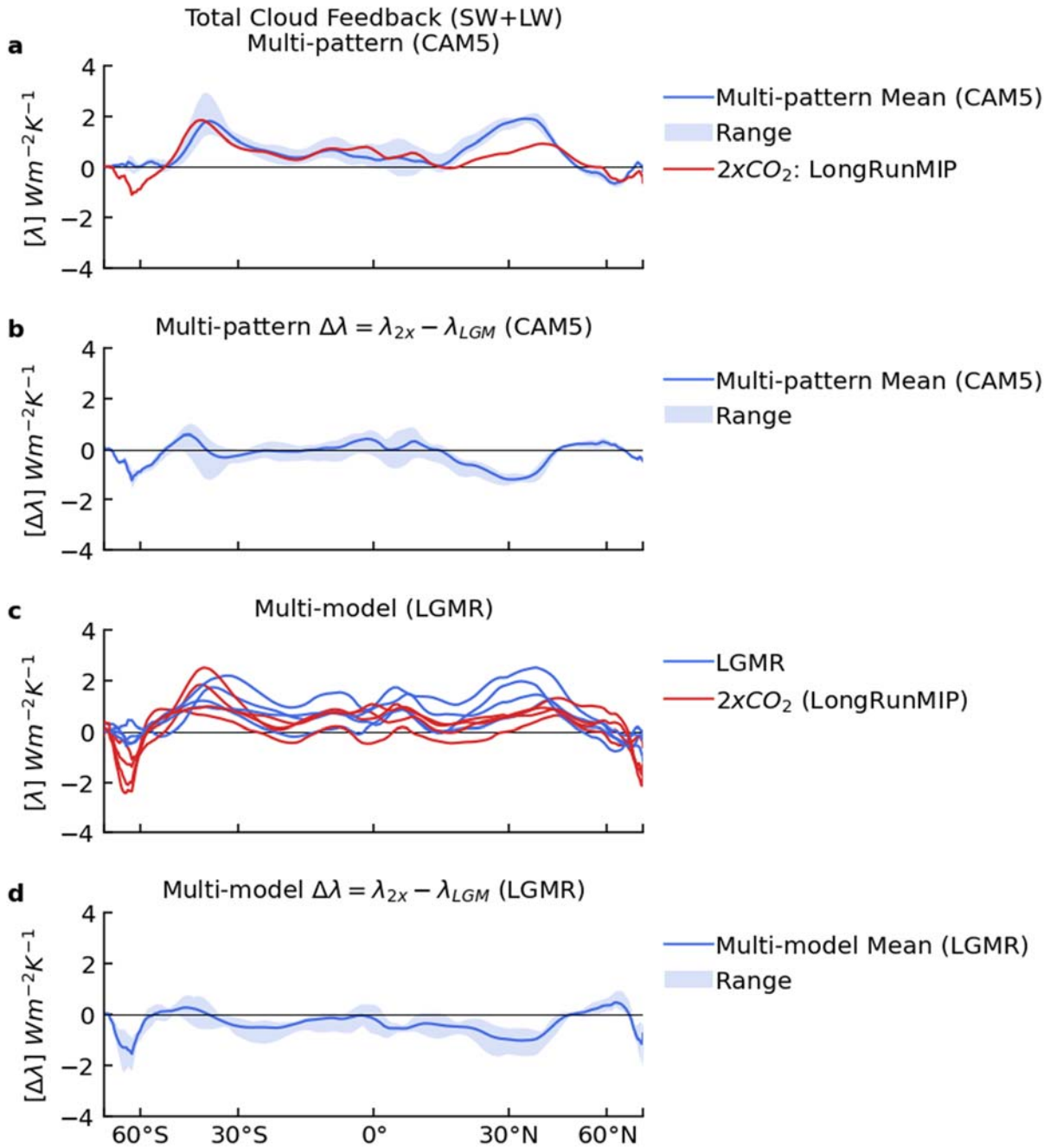
1300
1301
1302
1303
1304

SI Figure 5.9 | Cloud (SW) Feedback
Figure description at beginning of SI Section 5.



1305
 1306
 1307
 1308
 1309

SI Figure 5.10 | Cloud (LW) Feedback
Figure description at beginning of SI Section 5.



1310
1311
1312
1313
1314
1315
1316
1317

SI Figure 5.11 | Total Cloud (SW+LW) Feedback
Figure description at beginning of SI Section 5.